CHART Scientific Report 2022

FCC-ee Injector Study and the P^3 Project at PSI

S. Bettoni, P. Craievich, J.-Y. Raguin, M. Schaer, N. Vallis, R. Zennaro (PSI)

S. Doebert, J.-L. Grenard, A. Grudiev, B. Humann, A. Latina, A. Lechner, R. Mena Andrade, A. Perillo-Marcone, Y. Zhao, Z. Vostrel (CERN)

F. Alharthi, I. Chaikovska, V. Mytrochenko (IJCLab)

A. De Santis, C. Milardi (INFN-LNF)

on behalf of the CHART FCC-ee Injector collaboration

January 2023

This report provides an insight into the progress of the FCC-ee Injector Study collaboration in the framework of the CHART proposal over the past 12 months. The report is organised with a section for each work package to highlight the results achieved for each topic.

Contents

1 Overall Parameter Optimization (WP0) 4

1.1 Run time for Z pole operation 5

1.2 Pre-injector layout with a damping ring at higher beam enargy 6

2 Electron Source, Electron and Positron Linacs (WP1, WP2) 8

2.1 Electron Source 8

2.1.1 Status of the electron source simulations 8

2.1.2 Requirements for the electron source in top-up mode 9

2.2 Beam dynamics design of the electron and common linac 10

2.2.1 Single bunch simulations 11

2.2.2 Multi-bunch simulations . . . 19
2.2.3 Preliminary conclusions and summary . . . 20
2.3 RF design of the linacs . . . 23
2.3.1 Electron linac accelerating structure studies . . . 23
2.3.2 Maximum accelerating gradient . . . 23
2.3.3 Preliminary considerations on the positron linac integration . . . 24
2.4 Positron Linac Between Injector and Damping Ring . . . 26
2.4.1 Modeling . . . 29
2.4.2 Two Basic Layouts . . . 29
2.4.3 Beam Dynamics Along the Linac . . . 31
2.4.4 Energy Spread, Transverse Emittance and Damping Ring Acceptance . . . 33
2.4.5 Outlook . . . 34
2.5 Klystron Parameters and Linacs RF Modules . . . 36
2.5.1 Klystron Parameters . . . 36
2.5.2 RF Modules for the Positron Linac . . . 37
2.5.3 RF Modules for the Electron Linac . . . 37
2.5.4 RF Modules for the Common Linac . . . 39

3 Positron Source: Target and Capture System (WP3) 41
3.1 Positron production . . . 41
3.2 Positron Capture System . . . 42
3.3 Optimization Studies toward Better Performance . . . 46
3.3.1 AMD field profile . . . 46
3.3.2 RF structure length . . . 48
3.4 Radiation Load Studies for SC Solenoid-based Capture System . . . 51
3.5 Design and Integration of the FCC-ee Positron Source Target: Current Status and Challenges . . . 53

4 Damping Ring and Transfer Lines (WP4) 55
4.1 Damping Ring overview . . . 55
4.1.1 Dynamic aperture . . . 56
4.1.2 Longitudinal beam dynamics . . . 57
4.1.3 Injection/Extraction timing . . . 59
4.1.4 DR Layout upgrades . . . 59
4.2 Transfer Lines overview . . . 60
4.2.1 Positron extraction line . . . 61
4.3 Energy Compressor section . . . 61

5 PSI Positron Production (P^3) Project (WP6) 64
5.1 Component Overview . . . 64
5.2 Beam Dynamics . . . 64
5.2.1 Impact of Normal Conducting Solenoids . . . 64
5.2.2 Study of Targets of Conical Geometry . . . 64

5.3 Beam Diagnostics 65
5.3.1 Broadband Pick-Ups 65
5.3.2 Vacuum Chamber after Spectrometer 66
5.4 Installation and Timeline 67

References **68**

Publications and Conference Contributions **71**

Collaborators **72**

1 Overall Parameter Optimization (WP0)

In this chapter, we will summarise the most important changes in the parameters of the collider and booster rings that have had an impact on the design of the whole pre-injector complex compared to the one presented in [1]. Table 1 lists the target parameters at the end of the pre-injector complex. The total charge to be injected into the collider rings at each injection from the booster is about 4 nC and considering a transmission efficiency between the different accelerators, such as between the linac and the booster ring (BR) and the BR and the collider rings (CRs), of 80% then the pre-injector must guarantee a charge of about 5 nC at the pre-injector end. Figure 1 shows schematically

Table 1: Target parameters for latest baseline layout of the pre-inejctor for the Z pole in the collider. The bunch by bunch intensity will randomly vary 0 to 100%, depending on the intensity balance between the collider rings and bunch-by-bunch injection intensity fluctuation has to be within 3%.

Parameters		Unit
Injection energy	20	GeV
Bunch population	$3.12 \cdot 10^{10}$ (5.0)	- (nC)
Repetition rate	200	Hz
Number of bunches	2	
Bunch spacing	25	ns
Rms normalized emittance (x, y)	10, 10	mm mrad
Rms bunch length [mm]	1	mm
Rms energy spread [%]	0.1	%

the latest basic layout of the pre-injector complex, which involves a high-energy (HE) linac to boost the beam energy from 6 GeV up to 20 GeV and inject the beams directly into the BR without going through the Super Proton Synchrotron (SPS) ring. However, a comparative study will be made between using the SPS or HE linac as a pre-booster considering the operational impact, infrastructures, performances and costs. One of the

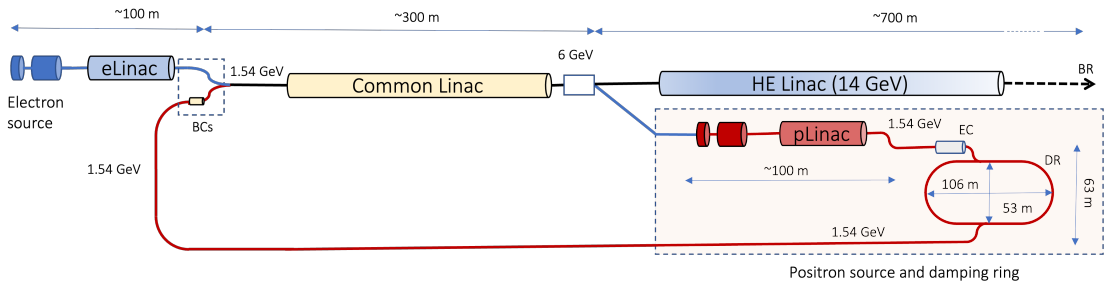

Figure 1: Latest baseline layout of the pre-injector complex including the high-energy (HE) linac.

parameters with the greatest impact on the pre-injector is the lifetime of the positron and electron beams in the CRs, which in the top-up mode involve an alternating injection

between the positron and electron beams about every 25 s. To ensure this specification, the pre-injector must operate at 200 Hz with two bunch separate 25 ns and this means operating the common linac during positron generation at 400 Hz. This requirement, as we will see in the following chapters, raises a serious challenge to the entire pre-injector complex for both rf technology, positron generation and damping ring (DR) operation. However, the top-up operation also still needs to be clarified in order to define the lower limit of the charge variation, which currently ranges from 0 to 100%. This requirement results from the different lifetimes of the individual bunches in the CRs, which will also determine the filling pattern for each injection.

The other parameters that have changed concern the injection parameters in the BR. First of all, the rms normalised emittance decreased from 50 mm mrad to 10 mm mrad in both planes for ensure a shorter cycle in the booster itself. This specification had an impact on both electron source and DR parameters. In particular, the electron source must guarantee this emittance value even during the required charge variation of the top-up operation, and this question, as we will see in Chapter 2, had a great impact on the optimization of the photo-injector.

Optimization of the BR is still in progress, and to make the design of the linacs in the pre-injector independent of that of the BR, an energy compressor [4] is planned to be installed in the transfer line from the HE linac to the booster, as shown in Fig. 2. With this approach, the design of the linacs can converge to a solution for the bunch length and energy spread at the linac end specified in Tab 1 without considering a compressor and/or beam decompression in the linacs, reducing the complexity of the pre-injector itself (see Chapter 2).

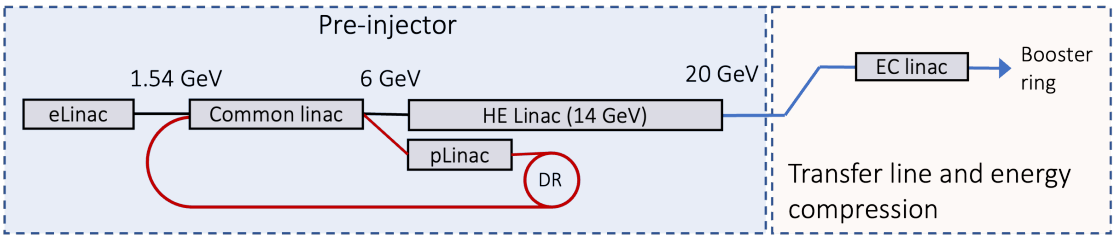

Figure 2: Schematic layout of the pre-injector complex and the transfer line to the booster ring including the energy compressor option.

1.1 Run time for Z pole operation

Among all the FCCee operation modes, the most demanding for the operation of the pre-injector is the operation with for the Z pole [2]. In [1], a filling mode of the collider was presented which involved the operation of the pre-injector at a repetition rate of 200 Hz (400 Hz for the common linac) and two separate 25 ns bunches. As mentioned above, this could also represent a challenge for the lifetime of the various components of the positron source due to the high rate of radiation produced by the target. One question that has arisen in recent months has been: How long will the pre-injector have

to operate in the Z-pole mode? As reported in [3], the operation of the Z-pole is expected to last four years plus the year of commissioning. This means that the operation time is 1.2e7 s per year of collisions. With the purpose of defining the specification for radiation shielding, an additional 25% operation time is estimated for CR filling, optimization, polarization, and reliability, and this leads to an operation time of the Z pole of about 1.5e7 s per year of positron generation. In addition, a charge of 10 nC will also be considered, which corresponds to a factor 2 higher than that shown in Tab. 1.

1.2 Pre-injector layout with a damping ring at higher beam enargy

As we will see in Chapter 3, the estimates of the positron yield are high compared to current positron sources. This higher yield has led to some considerations regarding the possibility of considering a higher-energy DR. The energies of the positrons, and thus of the DR, to avoid polarisation resonances are 1.54, 1.98, 2.42, 2.86, 3.30, 3.75 GeV etc., and a schematic layout considering a DR at 2.86 GeV is shown in Fig. 3.

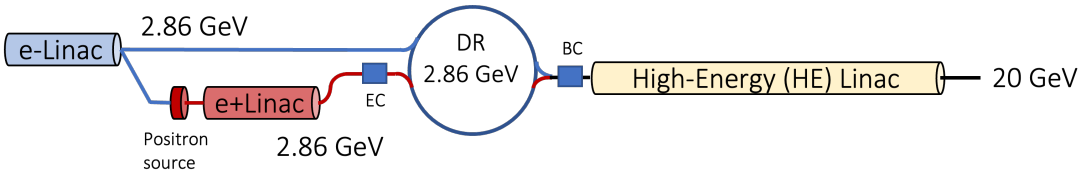

Figure 3: Schematic layout of the pre-injector with a damping ring at higher energy. linac. EC: Energy Compressor, BC: Bunch Compressor.

As reported in Chapter 3, the large increase in the positron yield, compared to other positron sources, is largely due to the larger apertures in the rf structures and the larger magnetic field provided by the Adiabatic Matching Device (AMD (see Chapter3). In practice, we have increased the acceptance of the positron source/linac system and moved the question downstream by placing more stringent specifications on the injection into the DR. Increasing the energy of the DR, thus with lower geometric emittance at the positron linac end, and reducing the energy of the driver beam, but with consequently lower positron yield, results in a more balanced system to ensure higher potential acceptance in the DR.

In addition, this approach allows all linacs to operate at 200 Hz with 2-bunch to meet the CR filling specification without having to provide for challenging 400 Hz operation of the common linac. A dedicated linac for electrons and positrons up to 2.42, 2.86 or 3.30 GeV leads to considerable simplification in operations while maintaining or reducing the total acceleration length. For example, simpler operation of the common linac in terms of seconds instead of milliseconds between positron and electron operations. Furthermore, with this approach, no positron return line is required and would also allow a higher charge from the electron source because the higher beam emittance could be damped in the DR as for positrons, see Fig. 3.

As a possible DR, considering synchrotron light source rings currently in operation

one could consider an energy of 2.8 GeV, a dipole magnetic field of 1.3 T for an angle of 3.5 degrees and have a DR with a circumference of about 300 m.

This approach would also allow for greater flexibility should one wish to propose a so-called flat beam with a vertical emittance much smaller than the horizontal one.

2 Electron Source, Electron and Positron Linacs (WP1, WP2)

The latest baseline layout of the FCC-ee injector complex is shown in Figure 1. It foresees two separate linacs for electrons and positrons up to a beam energy of 1.54 GeV – the eLinac and the pLinac, respectively. An advantage of this layout is that the solenoidal channel for the positrons in the pLinac can be extended without interruption beyond the exit energy of the former injectors (about 200 MeV in the CDR0 baseline). Switching to a FODO lattice at a larger energy can potentially increase the achievable positron yield and – at the same time – simplify the linac layout. As we will see in section 2.4, it might eventually be possible to directly switch from a solenoidal channel to a conventional FODO lattice, despite the huge emittance of the positron beam.

2.1 Electron Source

2.1.1 Status of the electron source simulations

The latest baseline layout of the injector complex (see Fig. 1) foresees a single electron source for positron and electron production. A first layout (see figure 4) of the electron source using an RF photo injector followed by an acceleration to about 200 MeV has been studied in detail [5]. It was shown that for the bunch charge of 3.2 nC the requirements for the beam could be fulfilled.

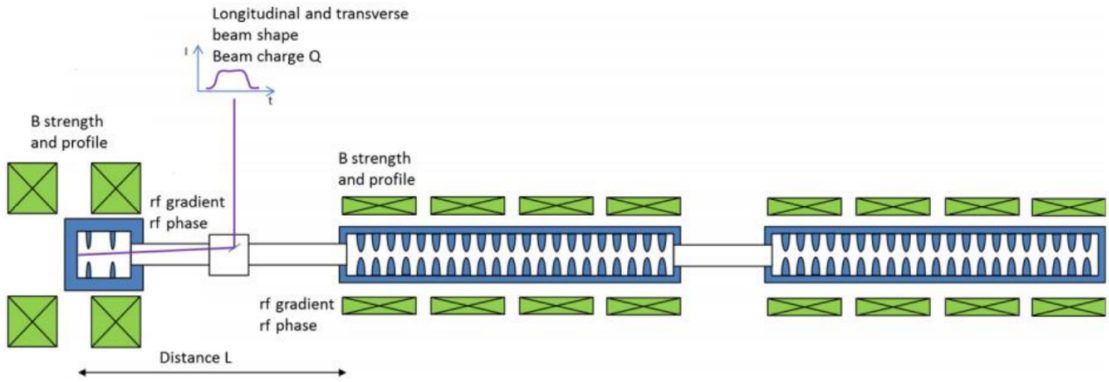

Figure 4: Conceptual layout of the electron source.

During this year the bunch charge has been increased to 5 nC per bunch and the emittance goal at the pre-injector end reduced to 10 mm mrad normalized transverse emittance following the requirements at the injection to the pre-booster ring. In addition, studies of the positron production yield indicate that 5 nC electron bunches for positron production are sufficient to reach the required positron bunch charge. Therefore, the electron source has been studied in the same configuration with 5 nC bunch charge. Both uniform and truncated Gaussian distributions have been studied, and the following beam parameters can be achieved at the end of the pre-injector at 200 MeV, satisfying the requirements, see Table 2. These parameters and the simulated distributions have been used as input for the design and simulations of the following injector linacs, which

accelerate the electron up to 1.5 and 6 GeV, respectively. During those studies (see following chapters), it turned out that a reasonably small energy spread is important, as well as a small bunch length, to not sample additional energy spread during acceleration. However, the following linac systems have enough flexibility to absorb higher energy spread and longer bunches. Nevertheless, a study has been done to investigate if the bunch length out of the pore-injector can be reduced. RMS bunch lengths down to 0.5 mm could be achieved but at the expense of transverse emittance. Since recently, the requirement for the transverse emittance was dramatically reduced to 10 mm!mrad it was decided to aim for a rms bunch length between 1 and 2 mm. This allows starting with a longer laser pulse on the cathode, which reduces the space charge forces and, as a consequence, gives access to smaller transverse emittances.
However, achieving reliably in day-to-day operation, such small emittances with a 5 nC bunch charge remains a challenge and requires very good control of the initial electron bunch distribution.

Table 2: Electron Source beam parameters at 200 MeV.

Parameter	Uniform Distribution	Gaussian Distribution
Transverse Emittance [mmmrad]	2	3
Energy Spread rms[%]	0.4	0.25
Bunch Length rms (mm)	0.98	1.3

2.1.2 Requirements for the electron source in top-up mode

One of the most challenging aspects of the FCC-ee electron source is the top-up operation mode for the collider. In this mode, the bunches circulating in the collider ring will be topped up with charge according to the charge erosion during a collision. Therefore the injector has to deliver varying bunch charges in the range of 10-100% for each bunch. Since we operate in a two bunch per rf pulse scheme with a distance of 15-60 ns it will be likely not possible to change the charge within these two pulses if the cathode is driven by only one laser. To enable this possibility, two independent lasers need to be foreseen. The source and the linac will work with a 200 Hz repetition rate, leaving 5 ms between pulses to adjust laser, RF or magnet parameters.
A detailed beam dynamics study has been started to determine which parameters need to be changed for different bunch charges to deliver as similar beams as possible. The best option would be to leave RF and magnet parameters constant and change only the laser spot size on the cathode so that the charge density stays as similar as possible. We believe the spot size could be manipulated fast enough using a controllable mirror array. Simulations show that, in this case, the beam parameter variation at the exit of the pre-injector is not to big (see Fig. 5). Further studies of these beams in the following linacs must be carried out before this option can be validated.

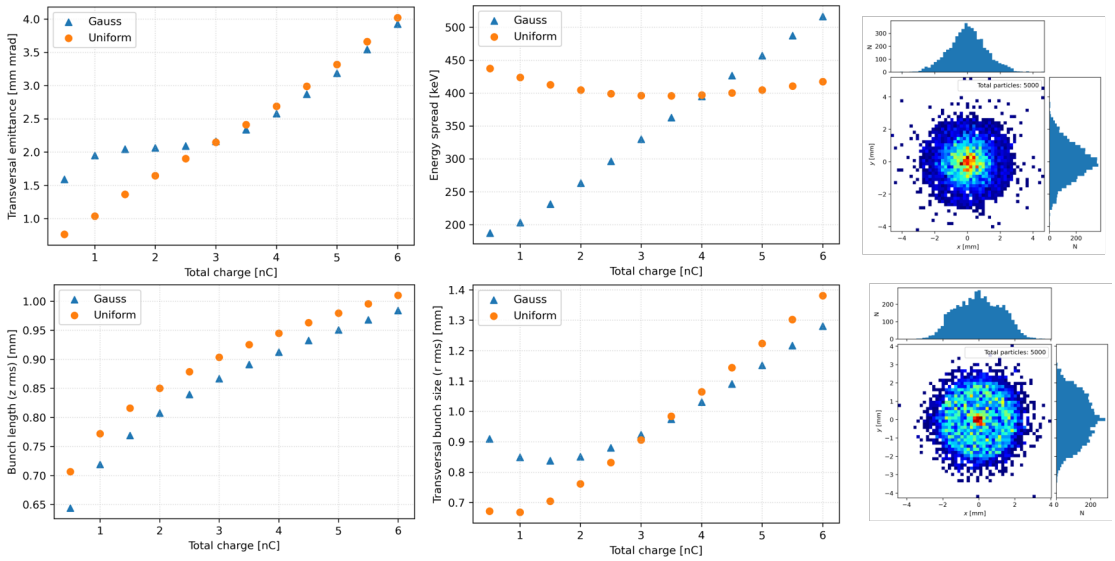

Figure 5: Beam parameter variation as a function of bunch charge simulating the top-up operation of the electron source and pre-injector.

2.2 Beam dynamics design of the electron and common linac

Electrons will be accelerated to the nominal 6 GeV by two linacs. The first linac, called electron linac, will boost the initial 200 MeV energy of the electron bunches coming from the injector from 200 MeV up to 1.54 GeV. At the latter energy, the electron bunches will share a second linac, the common linac, with the positron bunches coming from the damping ring. The common linac will bring the energy of both species to a final energy of 6 GeV. The main target parameters of this design are the final energy spread, which must be between 0.10% and 0.15%. A too-small or a too-large **energy spread** may be detrimental to the dynamics of the downstream ring. A too-low value may give rise to instability in the following ring, whereas a too-large one may reduce the dynamic aperture. Another parameter considered at the beginning of the design was the **bunch length**, which was supposed to be around 1 mm. This constraint was eliminated last year, considering that a compressor will be installed at the end of the linac to reach the target bunch length. We aim, in any case, to have a final bunch length of the same order of magnitude as required in the ring to minimize possible CSR (coherent synchrotron radiation) effects due to a large variation of the bunch length. This would also be an advantage if a high-energy linac substitutes the SPS to bring the bunches to 20 GeV and inject them directly into the booster ring. At such high energy, the compression system may become challenging also from the hardware point of view. Another essential part of the linacs design is the control of the **transverse emittance** growth, which aims to maintain the initial normalized transverse emittances of about 3 mm.mrad (from the electron source) to a value below 10 mm.mrad in both dimensions at the end of the common linac.

We used several numerical codes to perform the simulations: Elegant [6], mainly for the single bunch simulations, MAD-X [7] for the matching of the lattice, and RF-Track [8] for the single and multi-bunch simulations in the transverse plane. The latter code was developed at CERN by A. Latina. RF-Track was benchmarked against other codes, like Placet [9] and Elegant, and during this latest year, its author adapted and improved it to come up with the specific requests of the project.

In the following sections, we will summarise the results of the design work on the electron and common linacs, which was the baseline in the latest year. Preliminary simulations have also been done for the new configuration, where a high-energy linac in cascade to the common linac will bring the bunch's energy to 20 GeV before they are injected directly into the booster ring. These simulations are not reported in this report.

2.2.1 Single bunch simulations

We studied several effects in the longitudinal and transverse dimensions of the beams, considering the dynamics of a single bunch of each specie travelling along the linacs. In particular, for the longitudinal dimensions, we optimized the working point to reach the target energy spread with some considerations on the bunch length at the exit of the common linac. In the transverse dimension, we studied the possible emittance dilution due to static misalignments of the different accelerator components and the impact of the incoming orbit jitter at the working point determined by the longitudinal dynamics simulations. We included in the studies also the impact of the orbit correction on the emittance growth we observed.

Energy spread optimization The energy spread at the end of the common linac is given by the initial energy spread coming from the electron (or positron) bunch and the effect of the beam loading of the travelling bunches. When we speak about energy spread optimization in single bunch mode, we include in the studies the longitudinal short-range wakefield. Due to the relatively large charge passing through the linacs, this effect is quite important for the dynamics of the beam. We determined a working point of the linac, which produces the target energy spread at a bunch length determined following the criteria stated before.

In the simulations, we considered several scenarios, each having advantages and disadvantages. Their schematic view is displayed in Fig. 1. The first case we considered is the setup with a short pulse from the injector (the optimal value around 650 µm with respect to the nominal 1.3 mm at the end of the injector assumed when this optimization was started). In this option, the initial emittance is degraded (by about a factor 2 compared to the longer laser pulse), and the longitudinal space charge effect is increased. At the same time this configuration minimizes the hardware, and the emittance is not degraded due to CSR effects, since no compression ia applied to the bunch downstream of the gun section. The second option we considered was to use a bunch compressor along the electron linac. In this case, we can reach the smallest possible value of energy spread (equivalently, we have more margin to set the target value of the energy spread). As the main drawbacks of this scheme require more hardware, some possible emittance

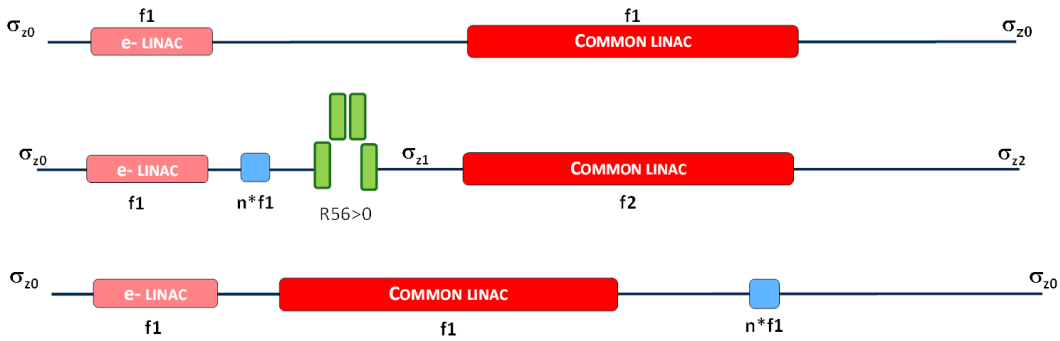

Figure 6: Possible schematic layouts for the electron and common linac.

degradation mechanisms due to the compression must be considered. We linearize the beam's longitudinal phase space in the third option without applying any compression. We do not have any possible CSR-related emittance growth effects, and we require some hardware but less than in the previous case.

To optimize these cases, we run 2D scans changing the bunch length and the operation phase of the common linac to produce a surface plot like the one shown in Fig. 7, where the colour code indicates the value of the energy spread at the exit of the common linac as a function of the initial bunch length and the operating phase of the rf structures along the common linac (we keep the electron linac on-crest for reasons related to the emittance dilution-see later). We considered several geometries that we labelled by a/λ, where a is the radius and λ the periodicity of the rf cavity, respectively.

Figure 8 shows the simulation results for the different considered layouts. All the configurations allow reaching the requirements, but the most interesting are those corresponding to the operation phase closer to the on-crest condition because of energy efficiency and in terms of possible emittance growth as well. For these considerations, we focused on the first kind of design. We enlarged the parameters domain by repeating the calculations for different frequencies of the rf structures (2 GHz, 2.8 GHz, and 5.6 GHz), geometries (a/λ equal to 0.1, 0.15, and 0.2), and gradients (25 MV/m and 40 MV/m). Figure 9 shows the maximum bunch length and the corresponding maximum operating phase of the common linac corresponding to a final energy spread of 0.1 % or 0.15% assuming the different rf parameters. This table allows us to compose the design in a modular way, and to draw some conclusions about the parameters space we may have for the different cases. The lowest frequency case of 2 GHz corresponds to an optimal bunch length of 1.2 mm rms, and an operation phase close to the on-crest phase. In the case that we will decide to add also a linearizer to this configuration (option 3 in Fig. 8) the frequency of the harmonic cavity at 6 GHz would correspond to a higher harmonic compared to the other cases, and this would be an advantage in terms of necessary power. For all these reasons from the beam dynamics point of view the solution at 2 GHz is the best one, but the rf efficiency (smaller shunt impedance) convinced us to disregard it. The other extreme case, assuming a common linac running

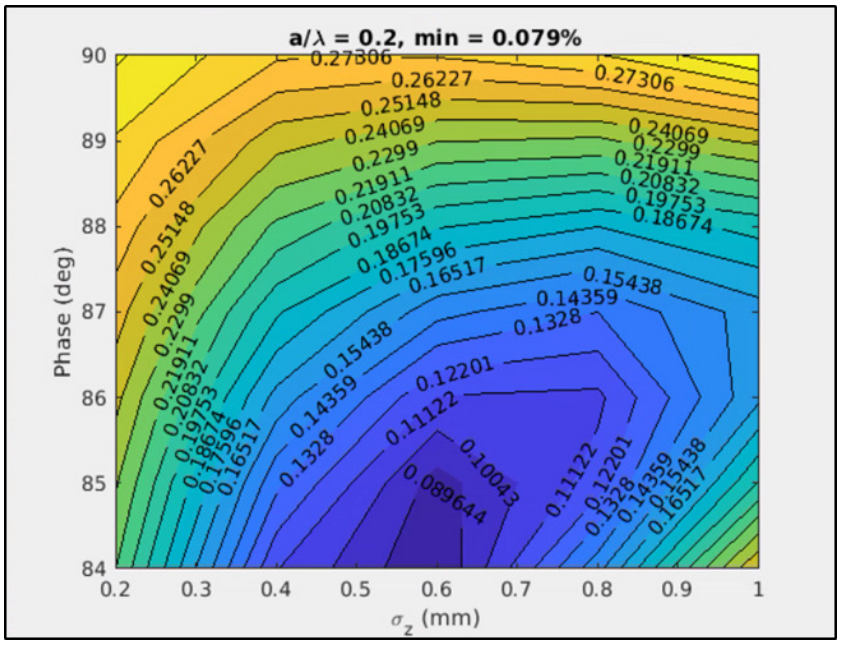

Figure 7: Relative energy spread at the end of the common linac example plot. The parameters we varied are the initial bunch length and the operating phase of the rf cavities. The colour scale corresponds to the energy spread at the exit of the common linac. The minimum value of the relative energy spread is indicated in the title of the figure. The on-crest phase corresponds to 90 degrees.

at 5.6 GHz, corresponds to an optimal bunch length of the order of 0.5 mm and an optimal operating phase quite far from 90 degrees. From the point of view of beam dynamics, this solution would be, therefore, the worst one. The intermediate solution of 2.8 GHz corresponds to an optimal operating phase quite close to 90 degrees, a bunch length around 0.7 mm, and a possible good rf efficiency. We are presently considering this latter case as the reference design. Figure 10 shows the number of structures needed to reach the target 6 GeV energy at the end of the linac for the two most promising geometries. The case with a higher gradient is the most efficient not only from the point of view of the hardware (fewer structures necessary to reach the target energy) but also from the beam dynamics aspects. In this case, in fact, also the beam loading is minimized (it scales with the total length of the structures), and the operating phase may be closer to 90 degrees, which has an advantage for the transverse dynamics as well. For the moment, we decided to select the conservative case of 25 MV/m at a/λ of 0.15 to perform more detailed simulations. After that, the geometry of the rf structures will be fixed the design will be optimized, and we will be able to select the correct value of the gradient and, therefore, precisely scale the number of structures. For the transverse space simulations discussed in the next section, we considered this case, if not differently specified.

1. SHORTER FROM THE GUN

	a/λ = 0.10	a/λ = 0.15	a/λ = 0.20
Phase range (deg)	73…74	<75…81	<80…85
Min δE/E	1e-3	5e-4	4e-4
Rms bunch length (mm)	0.8	0.4…0.65	<0.4…0.7

2. BUNCH COMPRESSION

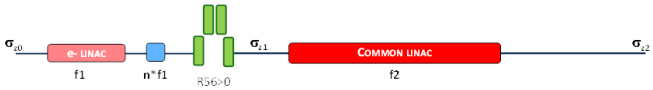

	a/λ = 0.10	a/λ = 0.15	a/λ = 0.20
Phase range (deg)	<70…75	86…>90	<80…85
Min δE/E	1e-4	1e-4	1e-4
Rms bunch length (mm)		0.457	

3. LINEARIZATION

	a/λ = 0.10	a/λ = 0.15	a/λ = 0.20
Phase range (deg)	66…70	77…81	81…85
Min δE/E	2e-4	3e-4	3e-4
Rms bunch length (mm)		0.650	

Figure 8: Summary of the performances of the possible scenarios for the common linac regarding the final relative energy spread. The minimum achievable energy spread, the corresponding bunch length, and the phase range where the energy spread is below the target 0.1 % value are shown for each geometry.

Emittance preservation: static misalignments The emittance along the linacs may grow due to an off-axis trajectory of the bunch along the quadrupoles (dispersion) and the rf cavities (short-range transverse wakefield). The maximum allowed emittance is 10 mm.mrad at the exit of the common linac. To simulate these effects, we misaligned these elements in both the transverse planes following a Gaussian distribution, and we computed the emittances at the end of the linac. We took some conservative assumptions, giving a rms of the misalignments of 50 µm and 100 µm for the quadrupoles and the rf structures, respectively. Figure 11 shows the typical analysis we apply to the results. We compute the histogram of the final horizontal and vertical emittances and determine the mean and the rms values of the distributions. We then calculate the fraction of the cases corresponding to final emittances below and above a certain value, as shown in Fig. 11.

Initially, we did these simulations using Elegant. We obtained a moderate emittance growth by applying Gaussian-like distributed offsets in the transverse planes and correlated misalignments. This growth became absolutely marginal when we applied a

f (GHz)	G (MV/m)	a/λ	a (mm)	Maximum σ_z (mm)		Maximum phase (deg)	
				δ_E = 0.1 %	δ_E = 0.15 %	δ_E = 0.1 %	δ_E = 0.15 %
2.8	25	0.1	10.7	0.8	1.2	69	89
2.8	25	0.15	16.1	0.8	1	79	82
2.8	25	0.2	21.4	0.7	0.8	82	82
2.8	40	0.1	10.7	0.8	0.8	77	85
2.8	40	0.15	16.1	0.7	1	82	79
2.8	40	0.2	21.4	0.7	0.8	85	84
5.6	25	0.1	5.4	No solution	No solution	No solution	No solution
5.6	25	0.15	8.0	0.5	0.6	61	66
5.6	25	0.2	10.7	0.5	0.6	74	66
5.6	40	0.1	5.4	0.4	0.5	81	73
5.6	40	0.15	8.0	0.5	0.5	71	72
5.6	40	0.2	10.7	0.4	0.5	67	72
2.0	25	0.1	15	1	1.2	78	81
2.0	25	0.15	22.5	1	1.2	85	85
2.0	25	0.2	30	1	1.2	84	86
2.0	40	0.1	15	1	1.2	87	88
2.0	40	0.15	22.5	1	1.2	86	84
2.0	40	0.2	30	1	1.2	88	87

Figure 9: Maximum bunch length and corresponding rf operating phase of the common linac for several rf parameters (gradient G, frequency f, geometry indicated by a/λ and the corresponding a) giving the target energy spread of 0.1 % and 0.15%, respectively. In case of the 2 GHz configuration the frequency of the electron linac is also 2 GHz, whereas for the other options the electron linac is at 2.8 GHz.

one-to-one orbit correction, assuming a reasonable value for the misalignments of the beam position monitors (BPM). We repeated the same studies with RF-Track intending to verify the results with a second and independent code. It came as a surprise that RF-Track gave a much larger emittance growth. We could verify that this discrepancy does not depend on the wakefields model, as it was still present even when we disabled their effect from the simulation. With RF-Track, we also observed that more off-crest operation phases of the rf structures lead to increased degradation of the beam emittance. Other codes, like Placet, confirmed the same observation. We contacted then M. Borland, the main developer of Elegant, to report this observation and verify the correctness

f (GHz)	G (MV/m)	a/λ	a (mm)	σ_z (mm)	N struct	Final E (GeV)	phase (deg)	Final δ_E/E (%)
2.8	25	0.1	10.7	1.0	63	5.94354	74	0.14145
2.8	25	0.15	16.1	1.0	62	6.07784	82	0.15331
2.8	40	0.1	10.7	1.0	38	5.94451	80	0.15482
2.8	40	0.15	16.1	1.0	38	6. 03897	85	0. 16159

Figure 10: Summary of the most interesting configurations of the common linac assuming several gradients and geometries of the rf structures. The choice among the two will be made once the transverse simulations are finalized with both the codes used for the simulations. The maximum energy used to determine the number of the structures is the closest possible to 6 GeV reachable, assuming a constant energy gain for all the rf structures and including the beam loading due to the short-range wakefield.

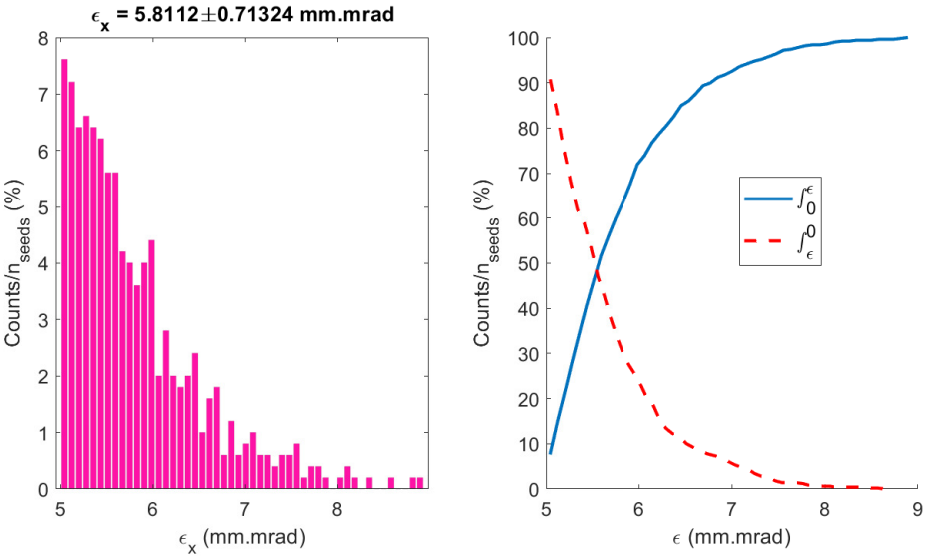

Figure 11: Typical outputs for the emittance studies due to static misalignments. Left plot: histogram of the emittance at the end of the linac. The graph's title indicates the mean and the standard deviation over all the seeds. Right plot: fraction of the seeds below (solid line) or above (dashed line) the emittance indicated in the abscissa.

of the results we obtained. Presently Elegant gives several possibilities to simulate the rf structures. The commonly used one in linacs for free electron lasers facilities, RFCW, allows simulating the effect of the wakefields on the bunch. Still, this element neglects the transverse field due to the off-crest operation phase of the rf cavity. Another one, TWLA, does not allow including the wakefields in the simulations, but it considers the transverse field depending on the off-crest operation mode of the rf structure. Following

this investigation done with M. Borland, we simulated the common linac in Elegant, and we compared the result obtained using RF-Track. The comparison result is shown in Fig. 12. It is evident that the effect neglected in RFCW is essential for our case. After

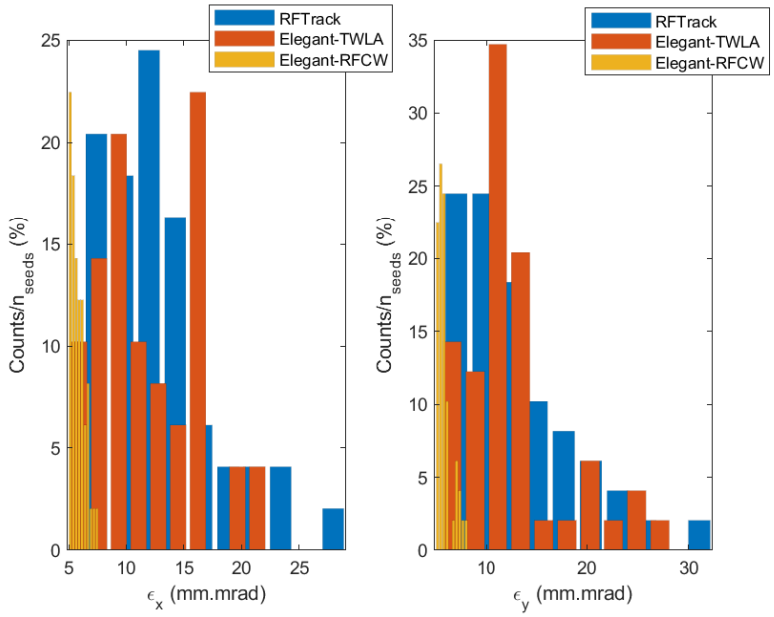

Figure 12: Comparison Elegant versus RF-Track using the different elements available to simulate rf structures in Elegant and RF-Track.

this finding, M. Borland promised to release soon a new Elegant version that simulates the rf structure, including both these effects, to describe the transverse dynamics of the beam better when the rf structures are operated off-crest.

As anticipated, unfortunately, we did the previous simulations using Elegant. In a relatively short time, we repeated the studies using RF-Track. A. Latina, the developer of RF-Track and one of the members of the FCC design group, has recently included the possibility of simulating orbit correction in the presence of misalignments. We are revising the linacs tolerances studies in single bunch mode for the electron, and the common linac previously performed using Elegant.

Figure 13 shows the histogram of the emittances at the end of the electron linac, assuming the quadrupoles and the rf cavities are misaligned, as stated before. The electron linac seems robust against the misalignments we introduced until now. The rf structures are operated on crest because we prefer to maximize the beam's energy as soon as possible and to minimize possible emittance growth mechanisms enhanced by the previously described effect related to the structures' operation phase. We applied the one-to-one correction (dispersion-free steering is available and to be considered in the future to improve the results further, if necessary), assuming that also the BPM (beam position monitor) are misaligned following a Gaussian distribution with an rms value of 30 µm to determine the emittance which could aim for at the end of this linac.

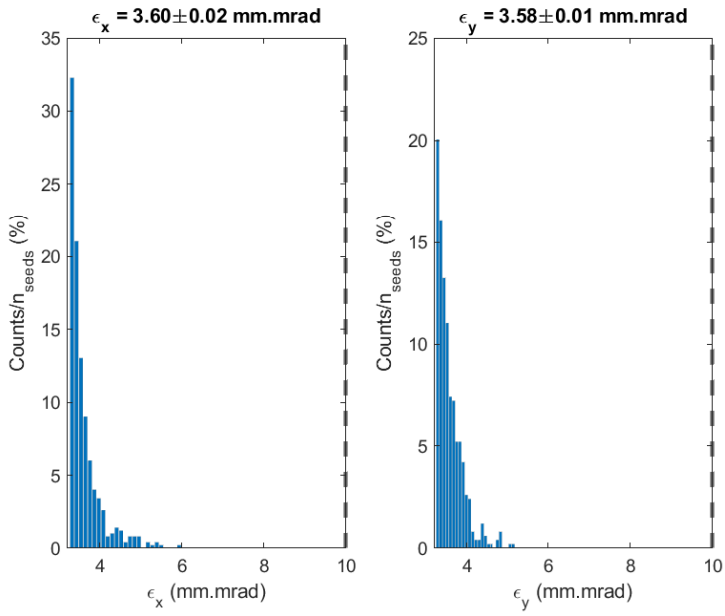

Figure 13: Emittance at the end of the electron linac due to Gaussian randomly misaligned quadrupoles (50 µm rms) and rf structures (50 µm rms). Case run with 500 seeds, misalignments distributed following a Gaussian distribution.

Figure 14 shows the results. As evident from Fig. 15, all the seeds correspond to a final emittance below the maximum tolerated value at the end of the common linac. In case we apply an orbit correction, only a very marginal fraction of the total emittance budget is used by this linac.

We repeated the same analysis to the simulations of the common linac. This linac is at higher energy than the previous one, but it is also longer, and the rf structures are operated moderately off-crest (8° from the on-crest phase). Figure 16 shows the analysis of the distribution of the final emittances referring to the common linac. In this case, the emittance growth is above the maximum tolerated value at the end of the common linac of 10 mm.mrad, and the orbit correction is essential, as shown in Fig. 17. Figure 18 shows the fraction of the seeds below a certain emittance value. From these simulations, it emerges that, with the misalignments previously stated and applying an orbit correction essential in the common linac, all the seeds are below the maximum emittance accepted at the end of the common linac.

Emittance preservation: jitter amplification Several jitter sources may be amplified when the bunch travels along the linacs: the arrival time, the mean energy, the charge, and the incoming beam orbit. Without a compressor, we do not expect a dramatic amplification of the time jitter; the mean energy also is expected to be not critical, and the charge jitter was previously discussed with an old linac design. We plan to perform all these analyses once the design will be finalized from the point of view of the

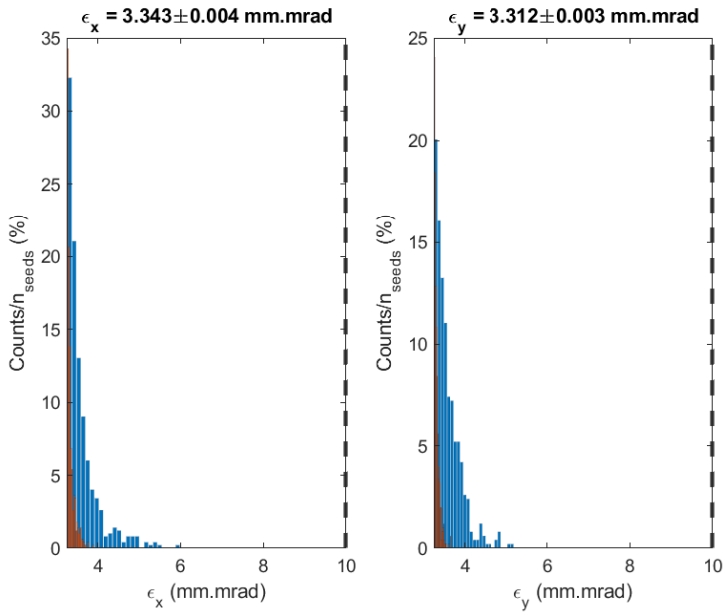

Figure 14: Electron linac: emittance at the end of the electron linac due to Gaussian randomly misaligned quadrupoles (50 µm) and rf structures (50 µm), and BPM (30 µm). The mean and rms of the obtained emittances shown at the top of the subplots correspond to the case of the steered beam. Case run with 500 seeds, misalignments distributed in a Gaussian distribution.

rf parameters. For the time being, we started from the expected most critical source of emittance dilution, which we expect to be due to orbit jitter.

We followed an approach proposed and presented in the past by A. Latina to do this kind of analysis. We determined the action, A, increase painting the bunch transverse phase space adding 10 % of the rms amplitude of the angle and position at the entrance of the linac. To study the tolerance of the rf structures geometry, we repeated the calculations assuming several apertures (a/λ). Figure 19 shows the obtained results. We arbitrarily took a maximum allowed amplification of 10 % compared to the initial action, as indicated by the dashed line. Considering this as the tolerated value, these calculations indicate that a value of a/λ equal to 0.1 is too small. A similar conclusion can be drawn for the case referring to the common linac, as seen from Fig. 20. This number will have to be compared with the action acceptable at the injection to the downstream ring, and eventually, the constraint will have to be tightened or relaxed.

2.2.2 Multi-bunch simulations

The two consecutive bunches of the same species separated by about 20 ns travelling along the linacs will interact via the transverse (and longitudinal) long-range wakefield. We imposed a kick to the second bunch to simulate this, and we computed the action

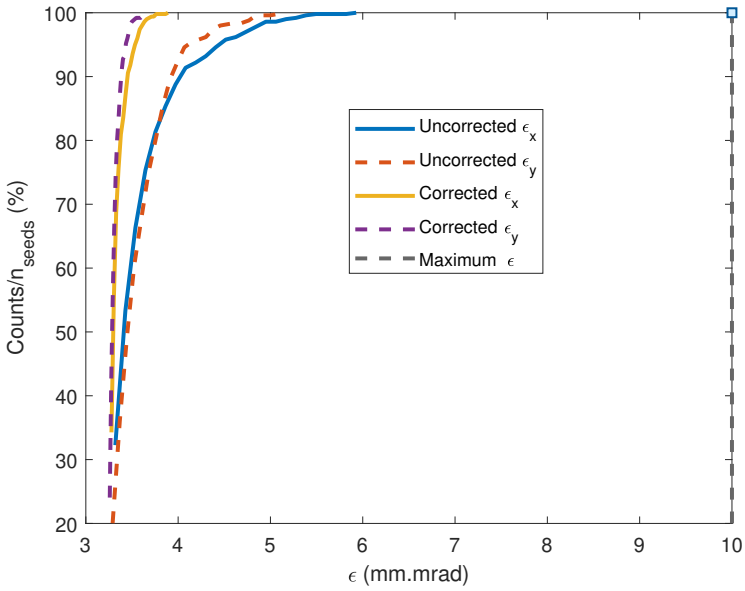

Figure 15: Electron linac: fraction of the seeds giving a final emittance below the value indicated in abscissa. The data refer to the cases used to simulate the common linac reported in the previous figures.

amplification painting the transverse phase space of the second bunch, as done for the single bunch before. In this way we determine a constraint on the maximum tolerated kick independently on the time separation among the bunches. We can give this number as input for the rf design. This way, we are independent of the possibly changing time separation among the bunches.

Figure 21 shows that the maximum tolerated kick is above 0.2 V/pC/m/mm, which is considered well achievable in the rf design, assuming the time separation of 17.5 ns among the two bunches.

Figure 22 shows that the common linac is even more forgiving since the tolerated maximum kick is about 30 % larger. This is because the beam is more rigid, so the same wakefield causes less beam degradation, even if the total length of structures is larger.

If 10 % action amplification is acceptable, from these simulations we can conclude that the long-range transverse wakefield is not an issue for the rf design, neither for the electron nor for the common linac.

2.2.3 Preliminary conclusions and summary

According to the simulations discussed in this chapter, we are converging to a design having rf structures at 2.8 GHz both in the electron and the common linac. Assuming a maximum 10 % action increase in both linacs for single and multi-bunch and a final maximum emittance of 10 mm.mrad a value of 0.15-0.2 for a/λ seems to be acceptable.

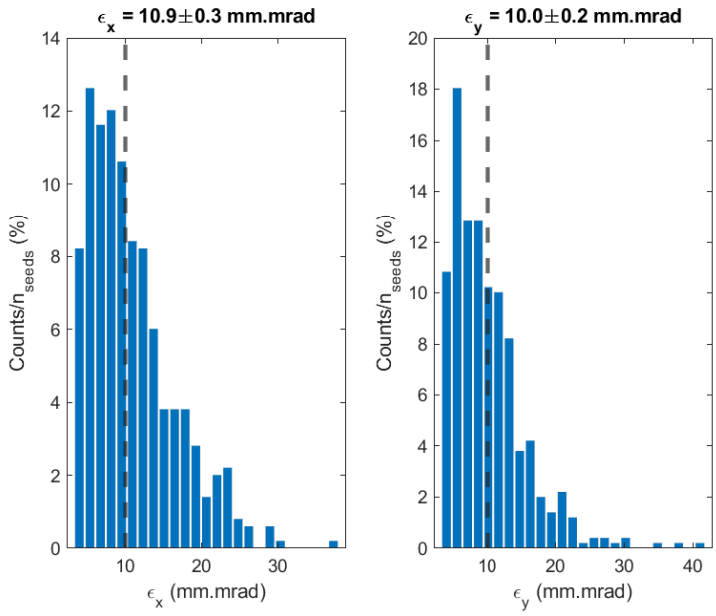

Figure 16: Common linac: emittance at the end of the electron linac due to Gaussian randomly misaligned quadrupoles (50 µm) and rf structures (50 µm). The mean and rms of the obtained emittances shown at the top of the subplots correspond to the case of the steered beam. Case run with 500 seeds, misalignment distributed in a Gaussian distribution.

This corresponds to a good compromise between the beam dynamics requests on the target energy spread, tolerance to jitter, and multi-bunch effects, and it would allow having a bunch length of the same order of magnitude as required in the downstream ring. As aforementioned, this will allow reaching the bunch length required by the downstream ring by applying a moderate compression factor. In this way, we may assume that the emittance should be only marginally affected by it.

During these studies, we identified a discrepancy between Elegant and RF-Track. After some investigations and with the support of M. Borland, we concluded that RF-Track, which gives less optimistic results and matches with other software like Placet in terms of emittance growth, is the software that better describes the reality for our cases. We have recently revised the single bunch emittance growth simulations using RF-Track to confirm the geometry of the rf structures. After this, the design of the rf structures can be fixed, their design optimized, and the resulting gradient determined. This will refine the beam dynamics simulations (correct length of the linacs/number of rf structures, etc...).

An issue not discussed in this chapter is the possibility of changing the bunch charge and keeping the bunches' properties in the specifications. Without applying any modification to the design, the different charge corresponds to different beam loading, which translates to different energy and energy spread at the end of the common linac. We

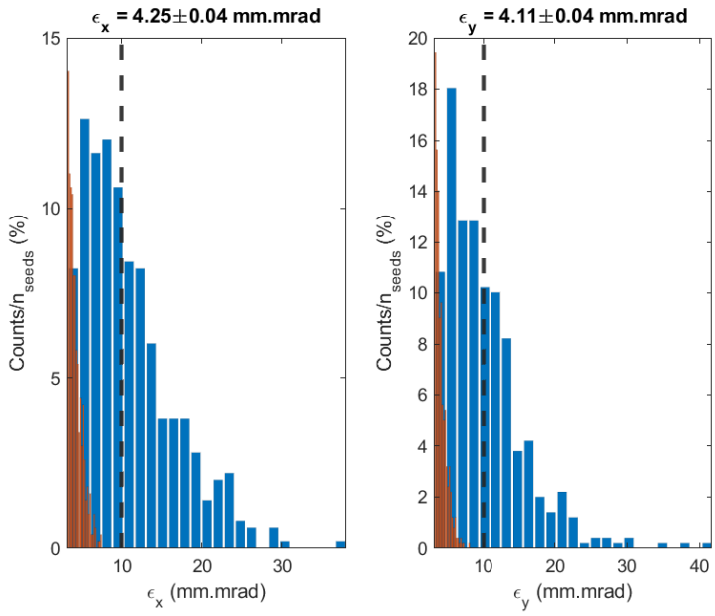

Figure 17: Common linac: emittance at the end of the common linac due to Gaussian randomly misaligned quadrupoles (50 µm), rf structures (50 µm), and BPM (30 µm). Gaussian randomly distributed. The distribution is determined over 500 seeds. In this case the mean and rms refer to the case of the steered orbit.

foresee installing an energy compressor between the end of the linac and the injection to the ring to cure this effect. The system, already applied in SuperKEKB consists of an element with a transfer matrix element R_{56} different from zero, which converts the energy separation among the first and the second bunch to time separation. The bunches travelling through an rf structure see different phases and experience different energy gains. We plan to use this system to compensate for the bunch-to-bunch energy difference and energy spread due to different charge operation modes. At the same time, we want to study a different operating phase of the common linac to use the same R_{56} of the chicane to match the final bunch length required for the booster ring.

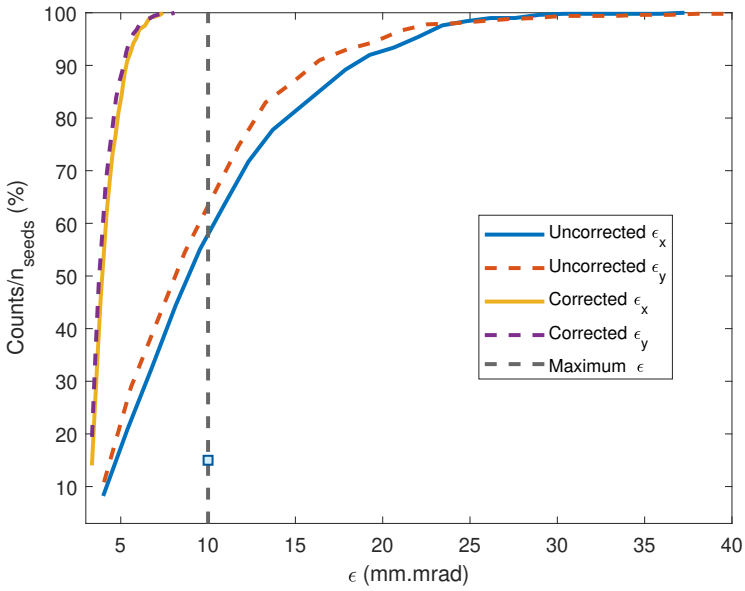

Figure 18: Common linac: fraction of the seeds giving a final emittance below the value indicated in abscissa. The data refer to the cases used to simulate the common linac reported in the previous figures.

2.3 RF design of the linacs

2.3.1 Electron linac accelerating structure studies

RF design of the accelerating structures for electron linacs has been investigated. Effective shunt impedance, which is the ratio of accelerating voltage square to the klystron output power has been used as a figure of merit. The effective shunt impedance versus structure length for different apertures is presented in Fig. 23 together with cell shape, which has been used in the study. A few selected structures are highlighted in Figure 23 by stars. The parameters of the highlighted structures are presented in Tab. 24 and considered in the possible linacs layout studies.

2.3.2 Maximum accelerating gradient

Vacuum breakdowns in high-gradient RF accelerating structures are known to be one of the main limitations in the high-power operation of linacs. In order to better understand the maximum accelerating gradient achievable in the stable operation of accelerating structures without RF breakdowns, the performance of the accelerating structures in a large range of parameters has been evaluated in terms of surface electric field Es and modified pointing vector Sc [10]. The range of parameters is defined here: rf phase advance $\phi = 2\pi/3$ - $9\pi/10$; frequency f = 2.0 GHz - 5.6 GHz; input and exit aperture radii = 0.08 λ - 0.34 λ; input and output iris thickness = 0.02 λ - 0.19 λ; structure

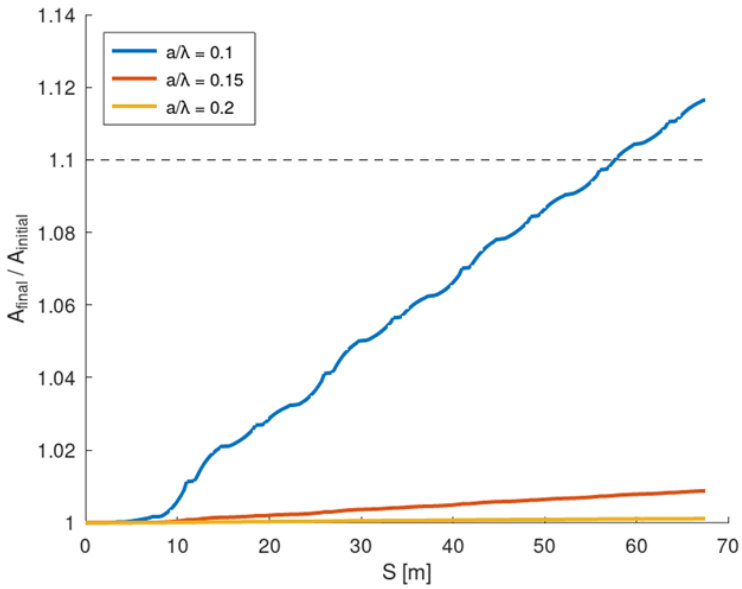

Figure 19: Action amplification as a function of the electron linac location for several geometries labelled by a/λ. The rf frequency is 2.8 GHz. The dashed line indicates the 10 % increase with respect to the initial values.

length L = 0.5 m - 5.0 m. In figure 25 maximum accelerating gradient achievable under two conditions is plotted. On the left, the condition is to stay below 100 MV/m surface electric field, which is one of the possible limiting values for high gradient operation. On the right, the condition is to stay below 4 MW/mm^2 od modified Poynting vector Sc which is another possible limitation of the high gradient operation. From the plots is clear that the one based on the surface electric field is more conservative and is chosen to define a maximum accelerating gradient of about 40 MW/m in the following studies of possible linacs layouts.

2.3.3 Preliminary considerations on the positron linac integration

Preliminary considerations on the possible integration of positron linac accelerating structure inside of focusing solenoids has been presented and discussed. The transverse layout is shown in Fig. 26 and longitudinal layout is shown in figure 27. The required dimensions for solenoids has been estimated: internal radius of at least 80 mm, length of large solenoid of about 2770 mm, distance between large solenoids of about 420 mm, length of optional intermediate solenoid of about 200 mm. This preliminary layout is used in both the beam dynamics and radiation dose and power deposition studies.

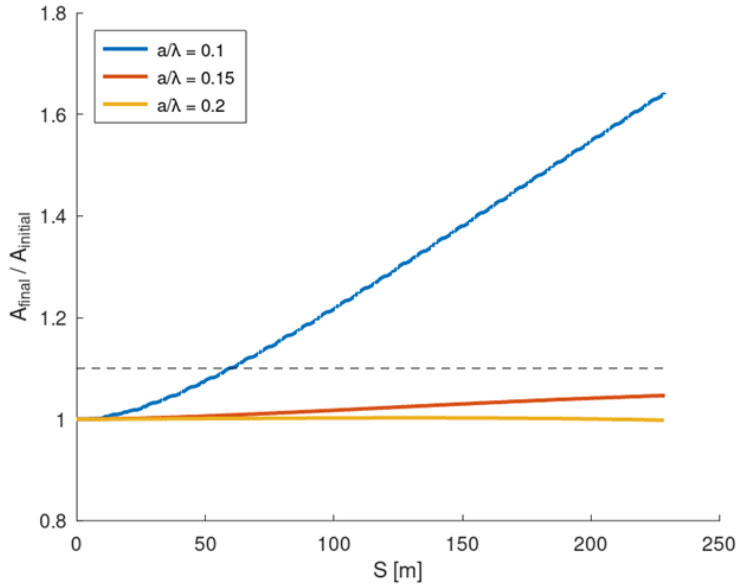

Figure 20: Action amplification as a function of the common linac location for several geometries labelled by a/λ. The dashed line indicates the 10 % increase from the initial values.

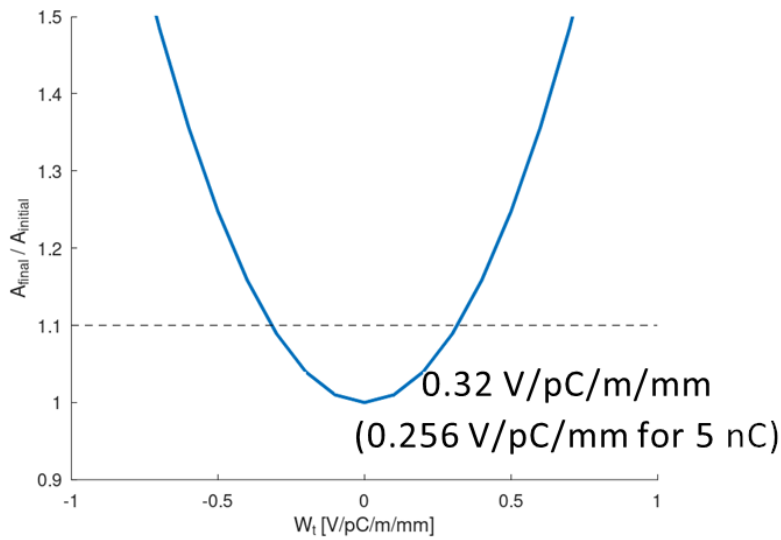

Figure 21: Electron linac: action amplification as a function of the kick due to the long-range wakefield acting among the two bunches of the same specie for two charge values (changing during the last year).

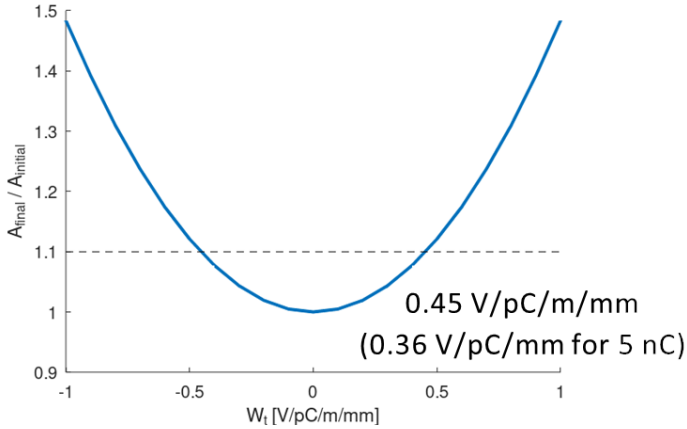

Figure 22: Common linac: action amplification as a function of the kick due to the long-range wakefield acting among the two bunches of the same specie for two charge values (changing during the last year).

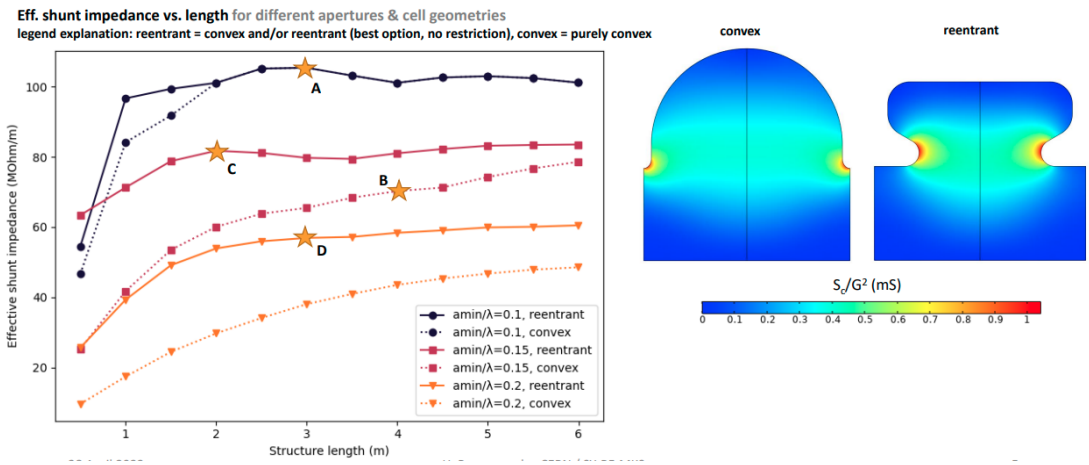

Figure 23: Effective shunt impedance of the accelerating structure versus structure length is plotted on the left for different apertures. Cell shape convex and re-entrant are shown on the right.

2.4 Positron Linac Between Injector and Damping Ring

After the positron production, collection and bunching in the capture system described in section 3 (WP3), the positrons must be accelerated up to 1.54 GeV, which is the design energy of the damping ring described in section4 (WP4). This energy boost takes place in the positron linac, or "pLinac" as it is indicated in the overall layout of the injector complex of Figure 1. Needless to say that strong interconnections exist between the design of the positron linac and the work done in WP3 and WP4.

The main achievement in 2022 related to the design of the positron linac has been the

	A	B	C*	D*
Frequency	**2.8 GHz**	**2.8 GHz**	**2.8 GHz**	**2.8 GHz**
Entrance aperture	**14.0 mm (0.13 λ)**	**18.4 mm (0.17 λ)**	**17.1 mm (0.16 λ)**	**22.9 mm (0.21 λ)**
Exit aperture	**10.7 mm (0.10 λ)**	**16.1 mm (0.15 λ)**	**16.1 mm (0.15 λ)**	**21.4 mm (0.20 λ)**
Phase advance	2π/3	5π/6	5π/6	9π/10
Length (num cells)	**3.0 m (84)**	**4.0 m (89)**	**2.0 m (44)**	**3.0 m (62)**
Geometry type	**Convex**	**Convex**	**Reentrant**	**Reentrant**
Entr., exit iris thickness	3.0 mm, 5.8 mm	6.1 mm, 6.1 mm	8.2 mm, 13.3 mm	11.2 mm, 14.0 mm
Transverse wake at 17.5 ns	0.22 V/pC/mm/m	0.21 V/pC/mm/m	0.19 V/pC/mm/m	0.19 V/pC/mm/m
Filling time	582 ns	497 ns	424 ns	428 ns
Min. group velocity	1.0 % c	2.2 % c	1.1 % c	1.9 % c
Largest cell radius	46 mm	48 mm	44 mm	44 mm
SLED coupling	14	15	16	15
Eff. shunt impedance	**104 MΩ/m**	**71 MΩ/m**	**77 MΩ/m**	**54 MΩ/m**
Average gradient	**25 MV/m**	**25 MV/m**	**25 MV/m**	**25 MV/m**
E_{max} (instant.)	80 MV/m	84 MV/m	100 MV/m	100 MV/m
$S_{c,max}$ (instant.)	640 mW/μm²	655 mW/μm²	719 mW/μm²	1003 mW/μm²
Klystron pulse length	3 μs	3 μs	3 μs	3 μs
Klystron power per structure	18 MW	35 MW	16 MW	35 MW

Figure 24: Table of parameters of 4 selected structures shown in Figure 23.

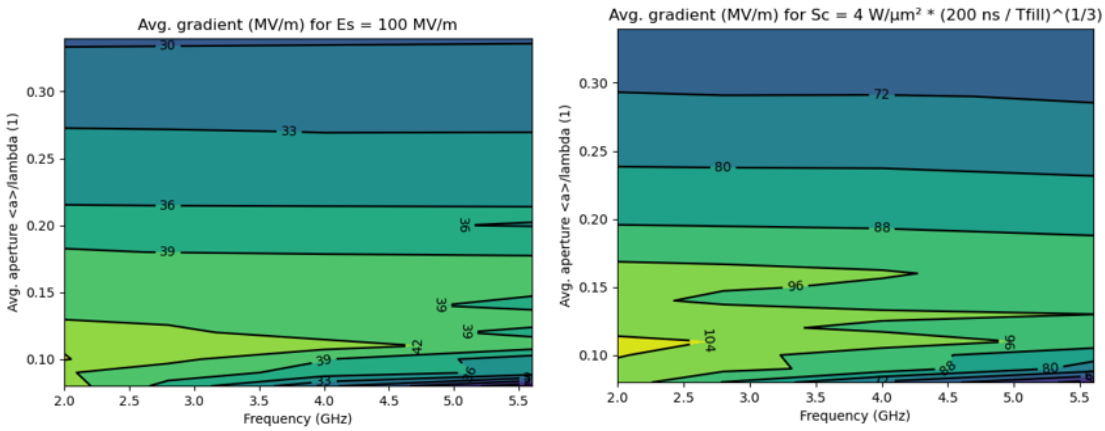

Figure 25: Maximum accelerating gradient predicted based on the maximum surface electric field (left) and modified pointing vector Sc (right).

setup of a start-to-end tracking simulation from the production target to the linac end, resulting in the development of a realistic linac design with good transmission, larger than 90 %.

The next fundamental step for the design of the capture system and positron linac

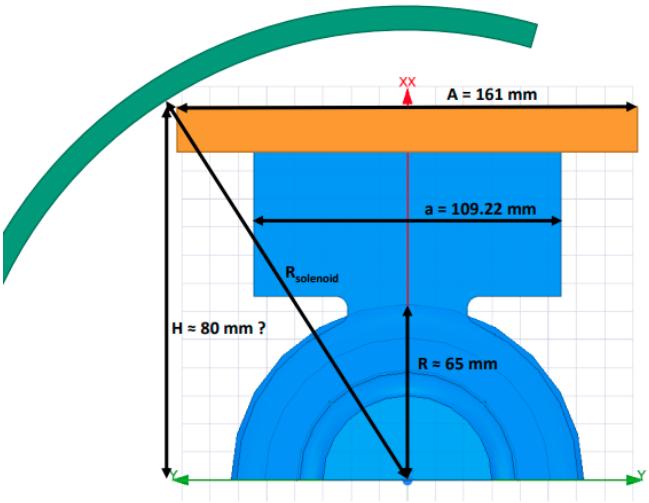

Figure 26: Preliminary design of the coupler of positron accelerating structure and its integration inside solenoids.

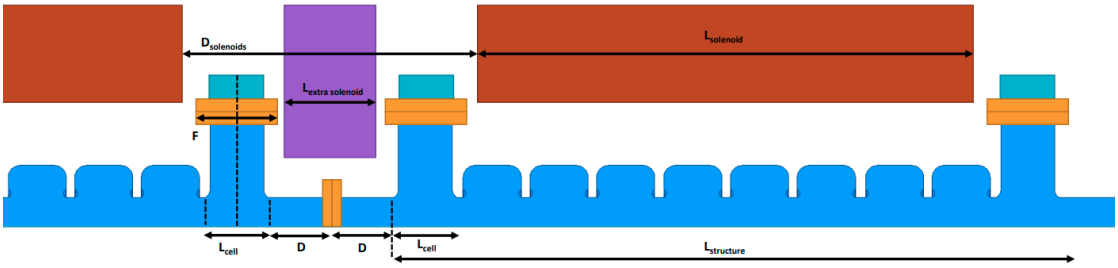

Figure 27: Preliminary integration of positron accelerating structure and the solenoids along the positron linac.

will be the computation of a first realistic positron yield after the tracking of the first turns in the damping ring (WP4). We will then face one of the two following scenarios:

- The positron yield fulfills the FCC-ee requirements, proving the feasibility of the injector complex with the proposed design. Future work would then purely be an optimization work.
- The positron yield does not fulfill the FCC-ee requirements. In this case, a re-design of at least part of the injector complex would still be necessary to proof its feasibility.

2.4.1 Modeling

The beam dynamics simulation is performed with the code RF-Track [8], which had been selected as the ideal tool for the tracking of large-emittance and large-energy-spread beams. Currently, 1D field maps are used to model the solenoids and the RF structures, which all have been carefully designed and simulated with specialized FEM codes (see section 2.3 for the RF design). Due to the very large beam size as compared to the apertures, the implementation of 2D rotationally symmetric field maps is already ongoing (see section 2.4.5). Quadrupoles are modelled as finite-length, ideal quadrupoles without fringe fields. Considering the large beam energy at which they are placed and their large spacing, this should be good enough for a feasibility study.

The full consistency between all parameters set/assumed in the simulations is ensured by a basic 3D mechanical model of the linac. In particular, collisions between RF couplers and solenoids as well as magnet apertures have been proofed. Some interesting details can be appreciated in Fig. 28, like the increase of the beam pipe radius from $r = 30$ mm to $r = 45$ mm in the matching section to reduce the positron losses, where the betatron functions reach values up to $\beta_y = 26$ m.

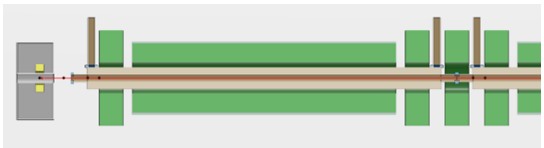

(a) Capture system section with high-temperature superconducting coils (yellow) and target (red), followed by an RF structure (copper) surrounded by the solenoids (green). This last unit repeats for the whole solenoids' section (Layout 1 and Layout 2).

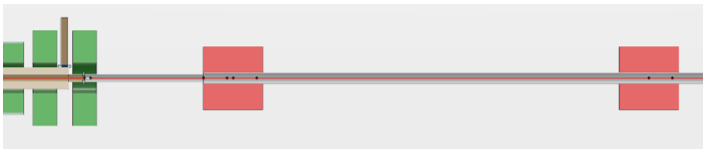

(b) End of the solenoids' section – start of the matching section (Layout 2).

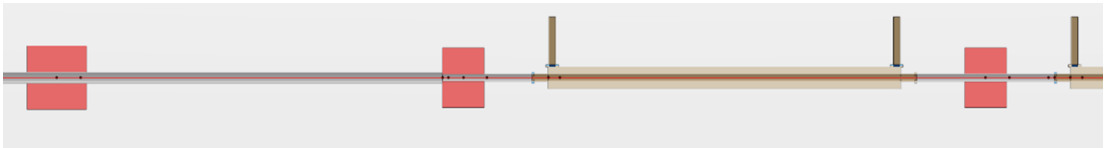

(c) End of the matching section – start of the FODO section (Layout 2).

Figure 28: Longitudinal cuts of the basic 3D mechanical model of the positron linac.

2.4.2 Two Basic Layouts

Start-to-end tracking simulations have been performed for two different linac layouts, whose main characteristics are presented in Tab. 3. The very first part of both layouts is nothing else than the capture system, which has been carefully optimized in WP3 as

described in section 3. The definition of a clear layout of the capture system – that has been named "Capture System -version 0" – has been very important in order to develop a first concrete proposal for the layout of the positron linac up to the damping ring. The adoption of a conventional FODO lattice above a certain energy in Layout 2 brings several advantages, making this layout the baseline for future improvements:

- The number and size of magnets is considerably reduced, and very likely also their power consumption. Consider that the electric[1] power consumption of the solenoids around 1 RF structure amounts to 128 kW.
- The introduction of steering and corrector magnets in a FODO lattice is much easier.
- The same is true for diagnostic devices or even diagnostic sections.
- Positron as well as electron bunches are generated in the capture system. The two spieces must be separated at a certain point by means of dipoles, i.e. interrupting the solenoidal channel. To resume a solenoidal channel after separation instead of starting a FODO lattice is not expected to bring any advantage.

The energy at which the separation will take place will play a central role for the choice of the linac layout. The matching section between solenoidal channel and FODO lattice in Layout 2 has been placed at 780 MeV in order to minimize the positron losses. The given normalized transverse emittance from the solenoids' section of $10'500$ mm mrad, the radial aperture of 30 mm of the selected RF structures and their length of about 3.240 m define – together with other parameters – the maximal value of the betatron functions along the FODO lattice. The selected energy of 780 MeV is the minimal energy providing maximal betatron functions which still allow to fit $F_a = 3$ sigmas of the transverse beam size within the beam pipe while having a quadrupole spacing of 4 m. This spacing allows to place the RF structures between the quadrupoles with a separation of about 390 mm between their flanges and the magnetic poles. This separation might seem large, but there is only a small reduction margin if one starts to consider bellows, vacuum valves and other devices. Fact is, that it will not be possible to lower the transition energy of 780 MeV remarkably.

All relevant parameters of the FODO section are collected in Tab. 4. The very large normalized transverse emittance of $10'500$ mm mrad coming from SolenoidSection1a is one of the starting parameters to design the FODO cell, together with the beam energy E and the number of transverse rms beam sizes F_a to be fit into the beam pipe of given radius R_a. The chosen phase advance $\Psi = 76.345$ deg keeps the upper limit of the betatron function along the FODO cell σ_+ as small as possible. As a rule of thumb, the length of the quadrupoles is always set to be 5 times their aperture (diameter), making them quite ideal magnets with a clear field plateau in their central part. This rule has also been applied for the quadrupoles in the matching section. More detailed considerations regarding the analytical scaling laws can be found in [1]. After the dimensioning with the

[1] To be doubled when considering cooling.

Table 3: Comparison of two basic layouts for the positron linac. The provided values includes all RF structures, solenoids and quadrupoles after the production target and HTS solenoid.

	Layout 1	Layout 2
	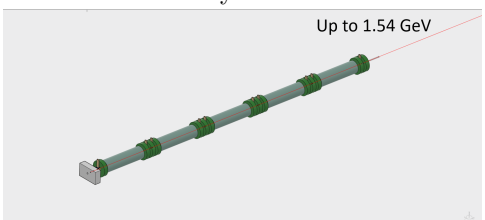	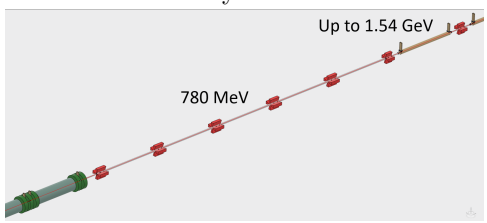
Description	Transport from the target up to the damping ring within an (almost) constant solenoidal channel of 0.5 T	Identical to Layout 1 up to 780 MeV, then matching section with 5 quadrupoles to a FODO lattice with constant cell length up to the damping ring
Section 1	SolenoidsSection1	SolenoidsSection1a
↳RF structure type	F3 @ 20 MV/m (presented in [11])	
↳No. of RF structs.	28	15
↳Solenoid types	Sol1a (long, with iron), Sol1b (short)	
↳No. of solenoids	28 × Sol1a, 84 × Sol1b	15 × Sol1a, 45 × Sol1b
Section 2	None	Matching1
↳No. of RF structs.	-	None
↳Quadrupole type	-	QuadMatching1 (large apert.)
↳No. of quadrupoles	-	5
Section 3	None	FODO1
↳No. of RF structs.	-	13
↳Quadrupole type	-	QuadFODO1 (standard apert.)
↳No. of quadrupoles	-	13
Overall length [m]	93	126

analytical formulae, the parameters of the FODO cell are refined with an optimization of the lattice in Elegant (see values in parentheses in Tab. 4).

The matching section Matching1 has also been designed in Elegant, with the main goal of keeping small betatron functions in order to maximize the transmission with reasonable beam pipe dimensions. In addition, a first, rough minimization of the matching section length has been performed.

All parameters determined with Elegant are finally implemented in RF-Track to perform the tracking simulation.

2.4.3 Beam Dynamics Along the Linac

Layout 1 demonstrates that it is in principle possible to accelerate the positron beam up to 1.54 GeV with minimal losses by confining the beam transversally with a homogeneous solenoidal channel. Note that the strength of the solenoidal field remains constant despite the increasing beam energy. This is possible due to the fact that the particles travel along

Table 4: Detailed parameters of the FODO section in the positron linac with Layout 2. The parameters in the first part of the table remain constant along the whole FODO section, while those in the second part vary. The values not in parenthesis have been computed from the known analytical formulae, while those in parentheses are the result of the more accurate computation of the FODO cell at 780 MeV with Elegant.

Constant along FODO	Radial aperture R_a [mm]	30	
	No. of σ_+ to fit F_a [mm]	3	
	Transv. emit. $\epsilon_{n,x}$ [π mm mrad]	$10'500$	
	Phase advance Ψ [deg]	76.345	
	Max. betatron func. β_+ [m]	14.537	
	Min. betatron func. β_- [m]	3.432 (3.488)	
	Cell length L_{cell} [m]	8.731	
	Focal length f [m]	3.532	
	Quad. length L_{quad} [m]	0.350	
	Quad. strength k_{quad} [1/m^2]	0.8090 (0.8245)	
	Pole radius R_{pole} [mm]	35	
	Drift length L_{drift} [m]	4.015 (4.052)	
Variable along FODO		Start	End
	Beam energy E [MeV]	780	1540
	Max. rms beam size σ_+ [mm]	10.000	7.117
	Min. rms beam size σ_- [mm]	4.859	3.458
	Quad. gradient G_{quad} [T/m]	2.105	4.156
	Pole field B_{pole} [T]	0.0737	0.1455

a spiral trajectory, whose radius only depends on the radial momentum and longitudinal magnetic field (Lorentz force in a homogeneous magnetic field). The radial momentum of the particles remains – in first approximation – unaffected by the acceleration in the RF field, which only increases the longitudinal momentum. This is reflected in an unconventionally constant transverse beam size along the whole linac and up to the final energy, as it can be seen (neglecting the post-processing artifacts) in Figure 29.

More conventional is the behaviour of the transverse beam size in Layout 2 where – after the matching section between solenoidal channel and FODO lattice in the range $z = 49 - 67$ m – we can recognize a typical betatron oscillation. Consider that the betatron oscillation cannot be ideal in this layout, since the beam energy is increasing along the lattice with constant spacing. This energy increase is compensated by a proportional increase of the field strength. Interestingly enough, the maximal transmission is obtained by tuning the optics for an energy of 75 % that of a virtual reference particle that is placed at the highest charge density in the longitudinal phase space and on the ideal trajectory (i.e. the beam axis) in the transverse. In Fig. 31 the virtual reference particle would lie in the yellow region around the point $(t, p_z) = (418.97 \text{ ns}, 1540 \text{ MeV/c})$. Despite the application of an individual tuning factor to the matching and the FODO section – resulting in the same optimal value of 75 % for both sections – losses of 8 % still occurs in the matching section, as it can be seen in Fig. 30. This seems to be unavoidable due

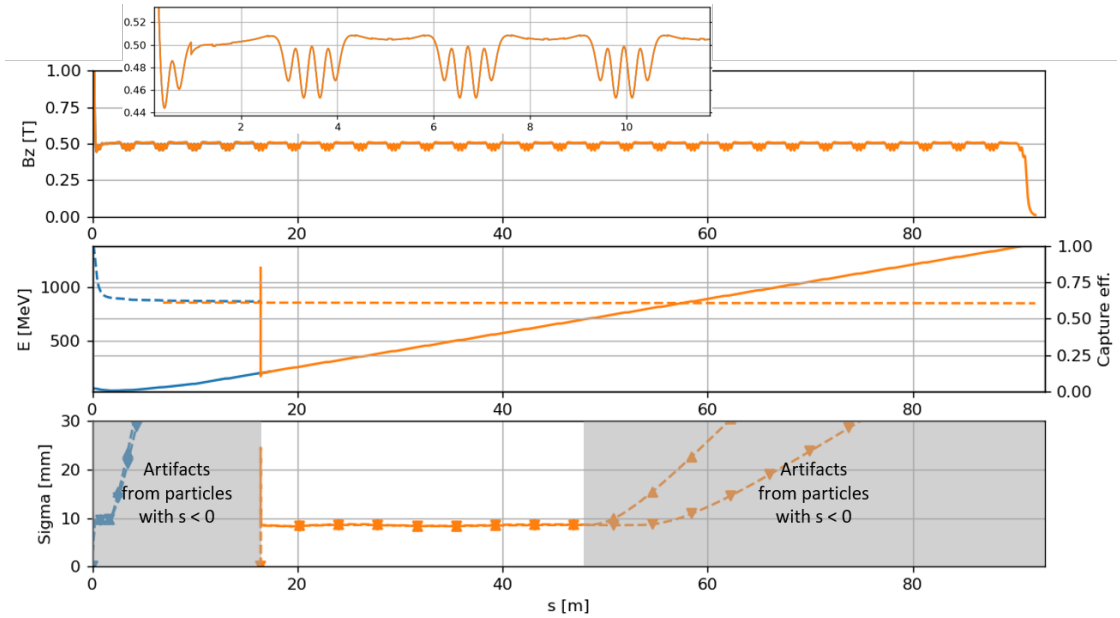

Figure 29: Evolution of the beam parameters along the positron linac for the Layout 1. Blue and orange lines indicate a 2-step tracking introduced for purely technical reasons (see e.g. bottom plot, where the post-processing artifacts are removed). In the top plot, the longitudinal magnetic field $B_z = 12.4$ T at $z = 0$ (target exit face) is out of scale. In the middle plot, solid lines refer to the left ordinate, dashed lines to the right ordinate. The spike around $z = 16$ m is a post-processing artifact. In the bottom plot, up- and downright triangles distinguish between the rms beam size σ in the x- and y-plane, respectively. Data points behind the gray regions are affected by post-processing artifacts and should not be considered.

to the extremely large normalized emittance larger than 10′000 mm mrad, even with an already large beam pipe radius of 45 mm.

2.4.4 Energy Spread, Transverse Emittance and Damping Ring Acceptance

For the first time, we are able to provide an accurate 6D distribution to the damping ring experts, who will track it further along the first turns of the damping ring for a first reliable estimate of the yield. Interesting considerations are already possible at this stage based on the simple assumption of a ±3.8 % energy window defining the longitudinal acceptance of the damping ring. This assumption is in fact still used for the optimization of the capture system in terms of yield at the damping ring. Applying the window in an optimal way as in Fig. 32, reveals an acceptance of 60 % of the main positron bunch delivered to the damping ring. In the transverse phase space (Fig. 33), the application of the energy window corresponds to a reduction of the emittance by about a factor of 2.

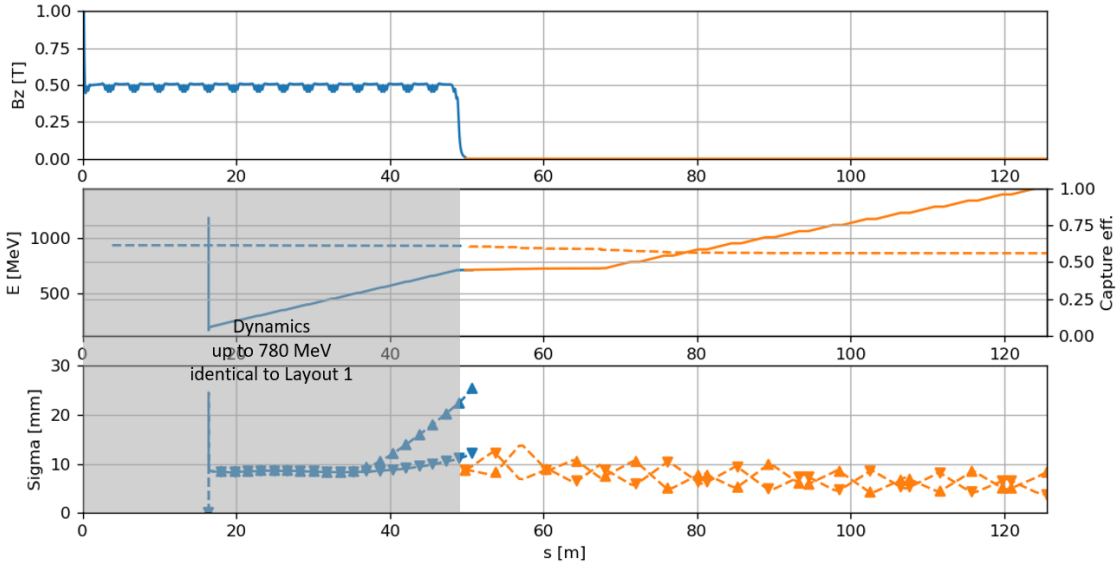

Figure 30: Evolution of the beam parameters along the positron linac for the Layout 2. Blue lines come from the tracking in "Volume" mode, orange lines from the tracking in "Lattice" mode. In the top plot, the longitudinal magnetic field $B_z = 12.4$ T at $z = 0$ (target exit face) is out of scale. Note that $B_z = 0$ in the second part of the plot is correct but misleading, since ideal quadrupoles are modeled in this region. In the middle plot, solid lines refer to the left ordinate, dashed lines to the right ordinate. In the bottom plot, up- and downright triangles distinguish between the rms beam size σ in the x- and y-plane, respectively. Data points behind the gray regions are affected by post-processing artifacts and should not be considered.

The last point might seem to be an advantage in terms of transverse emittance reduction, but it is not. In fact, an energy compressor to be placed after the positron linac has been designed, which allows to fit the whole positron distribution within an energy window of ± 2 %. This provides the possibility to accept the whole positron bunch into the damping ring, but requires the challenging handling of the full normalized emittance of $10'000$ mm mrad in the transverse planes.

2.4.5 Outlook

- Implementation of the full 2D RF field map into the simulation setup. Since the beam is basically filling the whole aperture delimited by the irises of the RF cells, the analytical expansion of the current 1D field map in the transverse direction might be prone to remarkable errors. This might have an influence on the remarkable increase of energy spread along the linac (see the final distribution in Fig. 31), which must be confirmed.

- Insertion of a chicane, dog leg or arc along the linac in order to separate electron

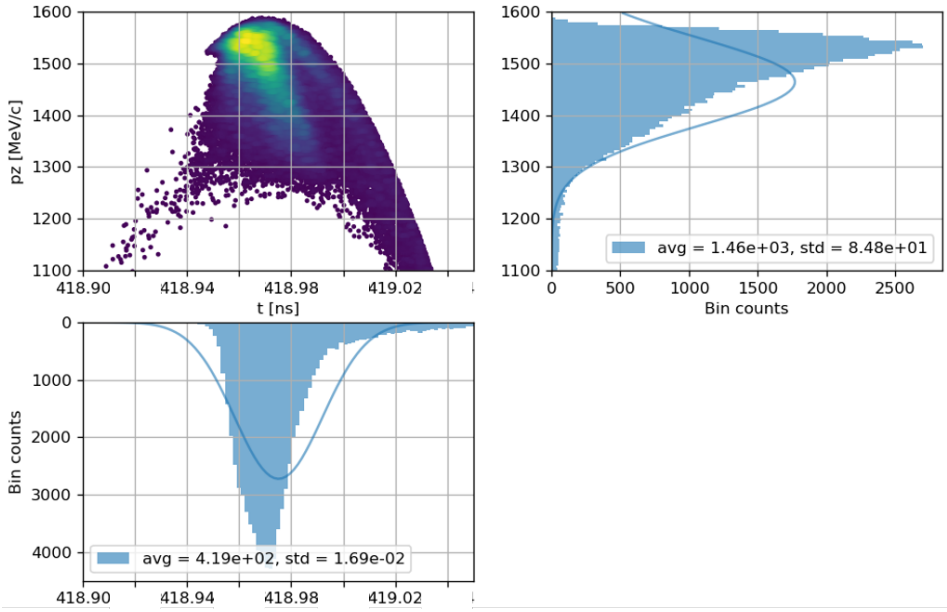

Figure 31: Longitudinal phase space of the main positron bunch at the end of the linac with Layout 2 (i.e. at about 1.54 GeV.

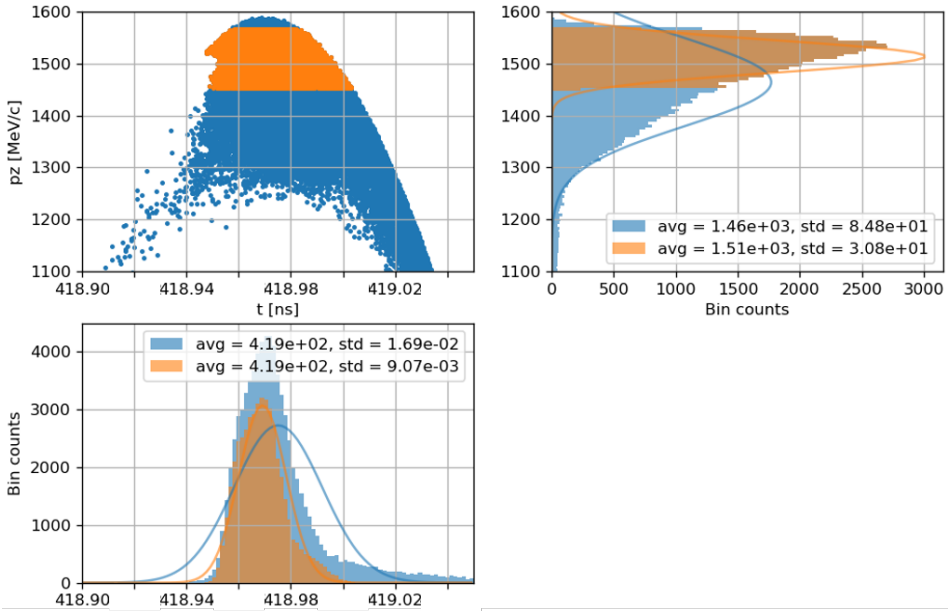

Figure 32: Longitudinal phase space accepted into the ±3.8 % energy window of the damping ring (orange) vs. full phase space of the main bunch (blue, same distribution as in Fig. 31) in the case of Layout 2.

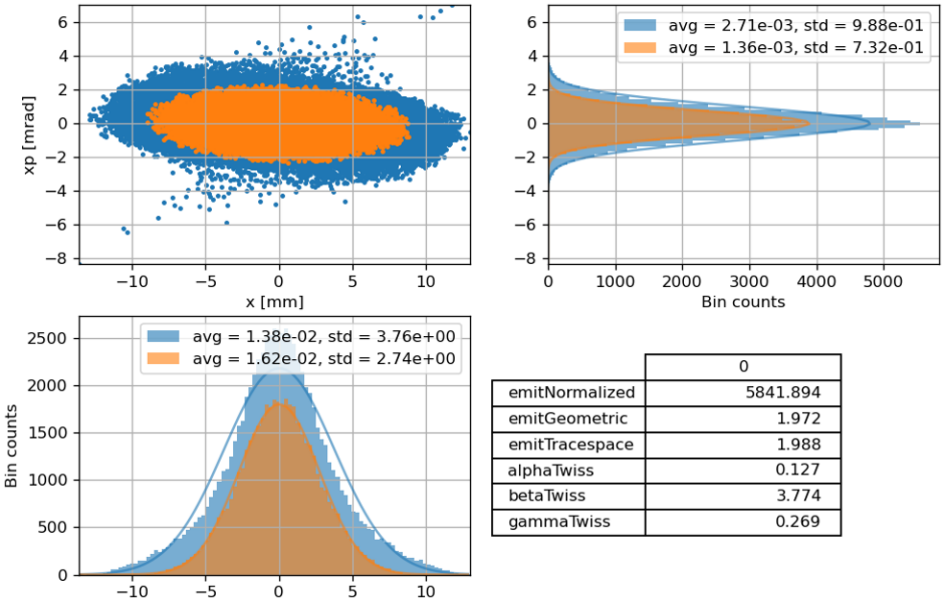

	0
emitNormalized	5841.894
emitGeometric	1.972
emitTracespace	1.988
alphaTwiss	0.127
betaTwiss	3.774
gammaTwiss	0.269

Figure 33: Transverse phase space accepted into the ±3.8 % energy window of the damping ring (orange) vs. full phase space of the main bunch (blue) in the case of Layout 2. The units in the bottom right table are consistent with those in the plots, i.e. mm and mrad are used. The values in the table refer to the orange distribution, to be compared with emitNormalized = 9′807 mm mrad of the full distribution (blue).

and positron bunches. In the Layout 2, the natural location for the separation would be the matching section at 780 MeV. At this energy, it should be possible to limit the positron losses to a small percentage. A separation at smaller energies – e.g. at 200 MeV – would be beneficial for the operation of the linac but would very probably be related to larger positron losses. A compromise needs to be found.

- Basic tolerance studies to verify the practical feasibility of the linac.
- (Eventually) Integration of the energy compressor reported in Section 4.3 in the RF-Track simulation, to achieve an even more comprehensive start-to-end simulation from the production target to the damping ring injection.

2.5 Klystron Parameters and Linacs RF Modules

2.5.1 Klystron Parameters

For the RF power sources i.e. klystrons, one of the technical challenges for the positron, electron and common linacs is the high repetition rates that are under consideration, 200 Hz for the position and electron linacs and 400 Hz for the common linac. Moreover, there is no klystron designed to operate at 2 GHz. At 2.8 GHz, although there are no klystron

at this specific frequency, many klystrons have demonstrated reliable performances at 2.856 GHz. Consequently, frequency adjustments on the klystron cavities would certainly reduce the development cost of such klystrons. The high average RF power resulting from higher repetition rates would be dealt with by redesigning the water cooling system of the klystron body and collector.

Several companies have been contacted to assess the feasibility of klystrons operating at 2 GHz, 2.4 GHz and 2.8 GHz. One of these companies provided us with peak RF power levels that could be achieved at repetition rates of 200 Hz and 400 Hz for an RF pulse length of 5 μs and 6 μs - see Tab. 5 for the 5 μs cases. For shorter pulse lengths, a reasonable assessment of achievable klystron peak power P_k is to apply a power derating to pulse length to the power -5/6 i.e. $P_k \propto \tau_k^{-5/6}$ where τ_k is the RF pulse length.

Table 5: Klystron parameters.

Frequency [GHz]	Repetition rate [Hz]	Pulse length [μs]	Beam voltage [kV] (typ.)	Peak power [MW]
2.0	200	5	400	80
2.4	200	5	400	80
2.8	200	5	400	80
2.0	400	5	380	71
2.4	400	5	380	71
2.8	400	5	290	36

2.5.2 RF Modules for the Positron Linac

According to Tab. 3, 28 2-GHz three-meter-long F3 type accelerating structures (Tab. 1 in [11]) are required to reach a positron energy of 1.54 GeV. A possible module layout consists in one modulator, one klystron with a 5-μs RF pulse length, one pulse compressor and two three-meter long structures. Assuming 15 % power losses in the waveguide system and klystrons operating at 90 % of their RF power specifications, the required number of modules is then 14. The klystrons RF power specification is about 79 MW, a value that looks achievable - see Tab. 5. The main parameters for this RF module configuration are summarized in Tab. 6.

2.5.3 RF Modules for the Electron Linac

As a first option for the electron Linac, the three-meter 2.8-GHz structure A of Fig. 24 with an exit and mimimum aperture of 0.1λ and a $2\pi/3$ phase advance is very attractive because it has the highest effective shunt impedance. For a klystron power of 18 MW and a 3-μs RF pulse length, an energy gain per structure of 75 MeV is achievable. An RF module would then consists of one modulator, one klystron, one pulse compressor and three three-meter long structures. To achieve an energy gain of 1.34 GeV in this configuration and assuming on-crest operation, 6 RF modules are required with a klystron

Table 6: Positron Linac RF modules.

Parameter	
Frequency [GHz]	2
Total energy gain [GeV]	1.54
Structures length [m]	3
Energy gain per structure [MeV]	≤ 60
Required number of structures	28
Number of structures per module	2
Required klystron power per structure [MW]	30
RF pulse length [μs]	5
Repetition rate	200
Klystron RF power specification [MW]	79
Average power [kW]	79
Required number of modules	14

RF power specification of about 71 MW (Tab. 7). With the above derating law, such a klystron is certainly feasible.

Table 7: Electron Linac RF modules - First Option.

Parameter	
Frequency [GHz]	2.8
Total energy gain [GeV]	1.34
Structures length [m]	3
Energy gain per structure [MeV]	75
Required number of structures	18
Number of structures per module	3
Required klystron power per structure [MW]	18
RF pulse length [μs]	3
Repetition rate	200
Klystron RF power specification [MW]	71
Average power [kW]	43
Required number of modules	6

As a second option, an other three-meter $2\pi/3$ 2.8-GHz structure structure of interest is presented in Ref. [11], Tab. 2. Its average aperture is 0.15λ, its shunt impedance is therefore lower than the one of the previous structure and, consequently, the required peak RF klystron power to achieve a maximum energy gain of 75 MeV per structure is higher and is 21.5 MW. The RF module has the same configuration than in the first option - one klystron, one pulse compressor and three three-meter long structures - but the klystron RF power specification of about 85 MW assuming here also on-crest

operation - see Tab. 8. Although this power requirement is significantly higher that in the first option, such a klystron is also certainly feasible. The cost of such an RF module would probably be the same as the one proposed in the first option.

Table 8: Electron Linac RF modules - Second Option.

Parameter	
Frequency [GHz]	2.8
Total energy gain [GeV]	1.34
Structures length [m]	3
Energy gain per structure [MeV]	75
Required number of structures	18
Number of structures per module	3
Required klystron power per structure [MW]	21.5
RF pulse length [μs]	3
Repetition rate	200
Klystron RF power specification [MW]	85
Average power [kW]	51
Required number of modules	6

2.5.4 RF Modules for the Common Linac

One of the salient features of the common linac is its operation at a 400 Hz repetition rate. Using the same 2.8-GHz, 0.15λ average aperture structure than the one for the

Table 9: Common Linac RF modules.

Parameter	
Frequency [GHz]	2.8
Total energy gain [GeV]	4.46
Structures length [m]	3
Energy gain per structure [MeV]	75
Required number of structures	62
Number of structures per module	2
Required klystron power per structure [MW]	21.5
RF pulse length [μs]	3
Repetition rate	400
Klystron RF power specification [MW]	57
Average power [kW]	69
Required number of modules	31

second option of the electron linac, the number of required structures to achieve a final

energy of 6 GeV is 62 - see Fig. 10. These structures would operate 82 degrees off-crest and an RF module could consist of one klystron, one pulse compressor and two structures. A 2.8-GHz, 400-Hz repetition rate klystron with a 5-μs RF pulse length and an RF power of 36 MW seems feasible - see Tab. 5 - and, with the above derating law for a 3-μs RF pulse length, a 55-MW klystron looks doable. However, the computed klystron RF power specification for this RF module is slightly more and is 57 MW. Table 9 summarizes the main parameters related to these common linac RF modules.

3 Positron Source: Target and Capture System (WP3)

Positron production is always an extremely important topic for any electron-positron collider. This is particularly true for future colliders such as FCC-ee, which are designed to operate at the extreme end of parameters, where a positron source with a high positron yield is required.

Thus, the high-luminosity circular collider FCC-ee will need a low-emittance positron beam with high enough intensity to shorten the injection time. A positron bunch intensity of 2.4×10^{10} particles is required at the injection into a booster ring allowing for a positron flux of 9.6×10^{12} positrons per second without any safety factor. This value is comparable with the accepted positron yield obtained at the SLC and positron yield foreseen at the SuperKEKB [12].

3.1 Positron production

Two methods are investigated for positron production for the FCC-ee to obtain the required performances.

The first one is based on a conventional positron source using 6 GeV electrons impinging on a 17.5 mm thick tungsten target. The bremsstrahlung radiation of the electrons in the field of the nuclei is converted in e^+e^-pairs. This scheme has been used for all the e^+e^- colliders (ADA, ACO, DCI, SPEAR, ADONE, LEP and also for the first linear collider SLC) [13]. The experience has been mainly successful. However, due to the high number of electrons in the short bunch of SLC, the breakdown analysis of the used target led to a limitation in the deposited power density expressed in J/g [14]. Its maximum value (PEDD), for tungsten targets, is about 35 J/g. Such limitation has some consequences on the incident electron beam size and the target thickness limitations.

A second approach is based on the production of a large number of photons in thin crystal targets oriented on their main axes. Electrons propagating in the crystal at glancing angles to the axes are channeled and emit a large number of soft photons due to the collective action of a large number of nuclei [15]. Such method has been successfully tested at CERN and KEK [16, 17, 18, 19]. These investigations led to a concept of so-called hybrid positron source [20] associating a thin oriented crystal with an amorphous converter and a sweeping magnet in between to sweep off the charged particles emitted in the crystal, allowing only the photons to hit the amorphous converter [21]. This approach involving the sweeping magnet is of great importance especially for the linear colliders, where the drive beam power can reach very high values. In such a way, for the FCC-ee positron source, two options (conventional and hybrid) are under consideration.

Meanwhile the conventional production scheme is currently assumed for the design studies, optimising the hybrid positron source for the FCC-ee is ongoing. Together with the INFN/Ferrara group, the simulation of the electromagnetic processes and photon radiation in the crystal is performed by using the in-house simulation code [22], which was recently validated in the energy range of interest [21]. This allowed choosing the optimum parameters for the crystal target: a 2 mm thick tungsten crystal fixed along $\langle 111 \rangle$ axes has been selected to be used as a photon radiator for the hybrid positron

source as the one, which provides a good photon yield, moderate values of photon beam divergence and energy deposition in the crystal.

Several options for the hybrid target are under investigation now (see Fig. 34).

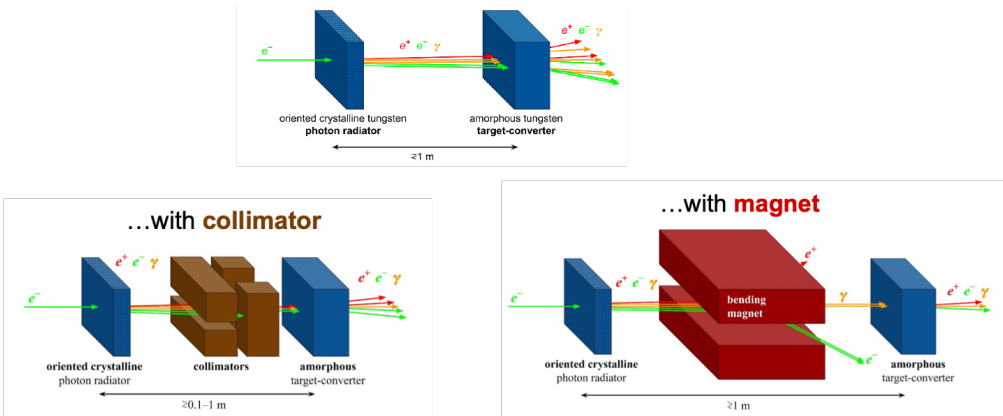

Figure 34: Options of the hybrid scheme for the FCC-ee positron source. Simple two-stage version, which features a crystal photon radiator followed by an amorphous converter (top), and optimized versions, in which a collimators or bending magnet is placed downstream the crystal (bottom).

As for the circular collider, the beam power is considerably lower compared to linear colliders, we started with the scheme without a bending (sweeping) magnet. Then, the options, including the collimators and the sweeping magnet were studied to compare the performances. The particle distribution coming from the crystal was used to simulate the positron production in the target-converter. The main results are shown in Fig. 35. The first results obtained are very promising. The studied schemes provide comparable positron production rates compared to the conventional target but lower PEED and power deposited in the target. Choosing the final configuration requires detailed positron capture simulations, being in progress now.

3.2 Positron Capture System

In order to perform the positron capture simulations the tracking codes such as ASTRA and RF-track are used.

The capture section comprises an Adiabatic Matching Device (AMD) [23] followed by the capture linac embedded in a DC solenoid magnetic field to accelerate the beam until about a few hundreds of MeV positron beam energy. Currently, we have assumed a 200 MeV, but studies are ongoing to define the energy at which the positrons could pass to the quadrupole focusing and be further accelerated up to the 1.54 GeV (energy of the DR). For the capture linac, several types of the RF structures have been considered up to now: 1.5 m long, TW 2 GHz L-band structures (2a = 40 mm), 3 m long, TW 2856 MHz S-band structures (2a = 30 mm), 1.5 m long SW 2998 MHz S-band structures (2a = 40 mm) designed for the P^3 project. Eventually, the 3-meter-long, TW 2 GHz

conventional (amorphous)
collimator
magnet

Scheme	conv.				hybrid			
L_{crys} [mm]	–				2			
D [m]	–	0.6		1			2	
L [mm]	17.6				11.6			
a = 5.5 mm Collimator?	no	no	no	yes	no	no	yes	no
Magnet?	no	no	no	no	yes	no	no	yes
E_{dep} [GeV/e^-]	1.46	1.34	1.32	1.13	1.32	1.27	1.11	1.27
PEDD [MeV/ (mm^3 · e^-)]	38.3	12.8	8.4	8.2	8.4	4.1	3.8	3.9
Out. e^+/e^-	13.7	15.1	15.1	13.6	15	14.9	13.7	14.9
Out. e^+ beam size [mm]	0.7	1	1.2	1.2	1.2	1.5	1.5	1.5
Out. e^+ beam div. [mrad]	25.9	27.4	26.8	27.7	28.9	29.2	25.6	27.1
Out. e^+ mean energy [MeV]	48.7	46.2	45.6	47.4	45.9	46.1	47.7	46.3
Out. n/e^-	0.37	0.31	0.31	0.27	0.29	0.29	0.26	0.3
Out. γ/e^-	299	310	308	270	307	301	268	301

Figure 35: Results for the positron production simulations in case of the conventional and hybrid production schemes. The results are given according to the options shown in Fig. 34.

(2a = 60 mm) RF structures designed by CERN for the positron linac have been chosen, providing larger iris apertures, which results in the larger transverse acceptance of the positrons. The accelerating structure interfaces and spacing require optimization as it strongly affects the accepted positron yield. Usually, the constant uniform solenoid field is assumed in simulation studies and recently, more realistic field profiles have started to be explored. However, the positron tracking up to 200 MeV showed a negligible reduction of positron capture efficiency compared to when the uniform field profile was used. This means that such assumption is fairly acceptable for several optimization studies of the capture system.

Two options are currently considered for the AMD: the first involves the use of a Flux Concentrator (FC), which makes use of a pulsed magnet, a technology presently used in the positron source of the SuperKEKB colliders [24], while the second involves the use of a SuperConducting solenoid (SC). The latter is based on the High-Temperature Superconducting (HTS) material with which the solenoid coils will be constructed. This technology will also be tested in the SwissFEL experiment at PSI (see chapter 5).

Several models of the FC have been designed and studied for the FCC-ee in BINP, giving the full 3D magnetic field map used for the simulations. The FC currently used in the simulation is 14 cm long with a longitudinal magnetic field starting at 7 T and adiabatically decreasing down to 0.5–0.7 T. The FC's front and rear aperture diameters are 8 mm and 44 mm, respectively. For the positron yield calculation, a gap between the target end and the nose of the FC of 2 mm was assumed. Due to the conceptual and mechanical constraints of the FC, the peak of the magnetic field is located downstream the target at a distance of 5 mm (see Fig. 36). As a result, the available field on the

target is reduced to 3 T manifesting a significant drop in capture efficiency. Moreover, the presence of a high transverse magnetic field component (with strong domination of dipole harmonic) makes the trajectories of positrons strongly distorted. As a result, the positron beam receives an offset in vertical and horizontal planes. This eventually should be mitigated for the positron beam transport in the capture linac.

In this framework, it was proposed to explore the use of an SC solenoid based on the HTS technology for positron capture. The comparison of the FC and the HTS field profiles used for the current studies is illustrated in Fig. 36. The HTS field map

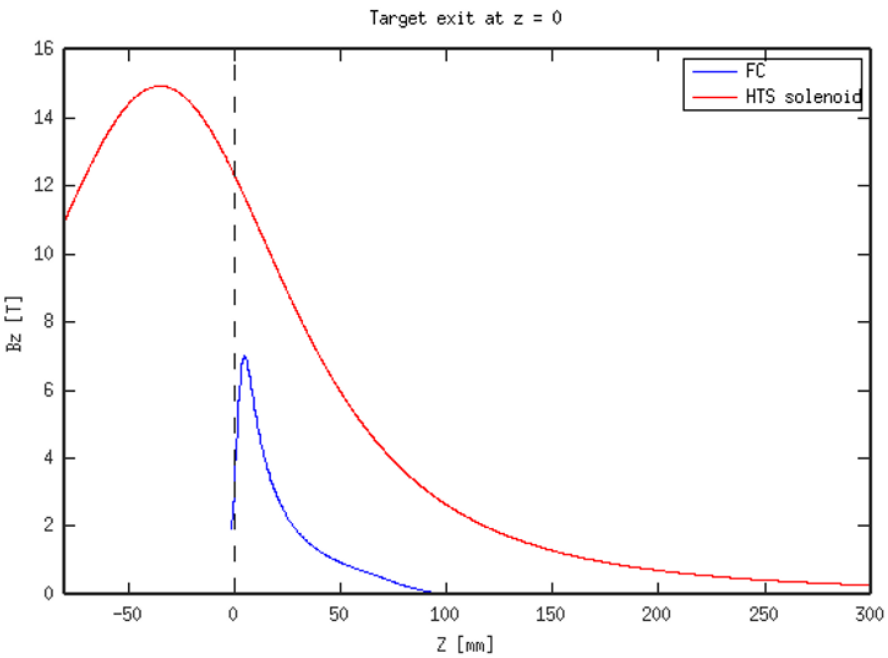

Figure 36: Magnetic field profile of the AMD realized in form of the FC and HTS magnet with the peak value located upstream or downstream of the target for the HTS magnet and FC respectively. The target exit surface is shown as a dashed line.

is adopted from the P^3 project. The HTS solenoid used as the AMD provides much higher field value on the target exit surface, larger aperture and flexible target position as the target can be placed inside the magnet bore. Thanks to the axial symmetry of the solenoid, the transverse magnetic field at the magnet axis is equal to zero and, therefore, no beam distortion is expected compared to the FC option. The evaluation of the final performance and cost for the FC-based and HTS-based capture systems are ongoing.

Based on the obtained results, the following capture system, so-called Capture System –version 0, has been defined to be used as a starting point for further investigations and optimizations and also, as an input for the positron linac studies (see Fig. 37). Hence, the Capture System -version 0 can be described as follows

- Positron production: conventional scheme.
- Matching device is based on the SC solenoid (5 HTS coils, 72 mm bore aperture including shielding)
- Capture linac is based on the L-band TW RF structures (2 GHz, 3-m long accelerating structures)
- NC solenoid with the field of B = 0.5 T (uniform or realistic field profile) is assumed for the capture linac.

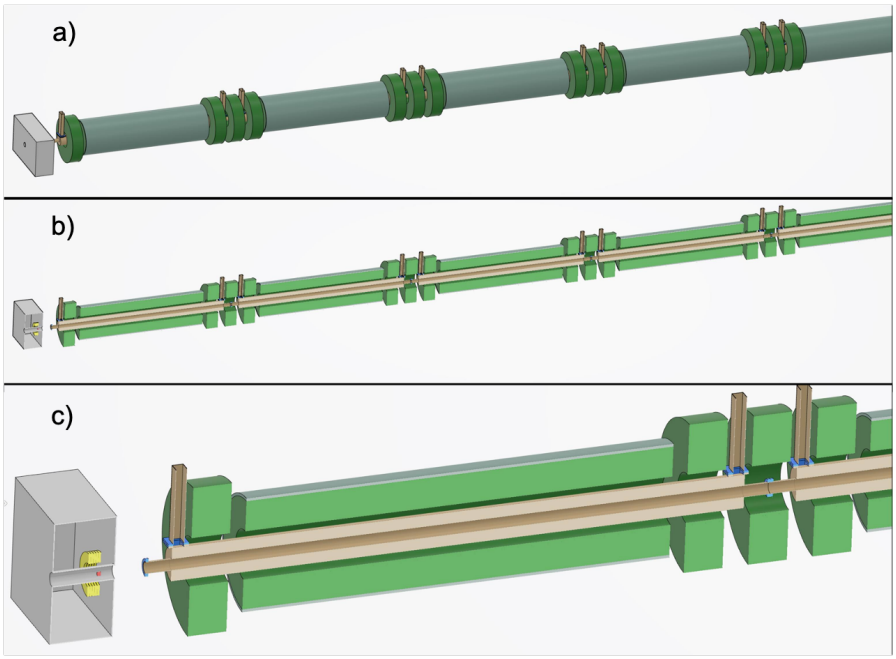

Figure 37: General layout of the Capture System –version 0. (a) The main view, (b) side cut into the capture system and (c) zoom of the cryostat contained the HTS coils and the first RF structure.

In this context, Fig. 38 shows the electric field of the accelerating structures and magnetic field profile along the whole Capture System -version 0. Thus, Tab. 10 summarizes the main current results of the positron production and capture simulations for both, FC- and HTS solenoid-based capture systems. At this stage, an energy-longitudinal position cut around the highest density of positrons made within the DR acceptance allows defining the accepted positron yield[2]. Later on, the positron tracking simulations in the positron linac followed by the injection in the DR should be carried out to have more realistic estimate of the accepted positron yield. Beam dynamics simulations have shown that both schemes can guarantee positron production even with some safety margin.

[2]For the results presented in Tab. 10 the energy window cut of ±3.8% and longitudinal position window of 16.7 mm (or 40 degrees in terms of the phase) have been used.

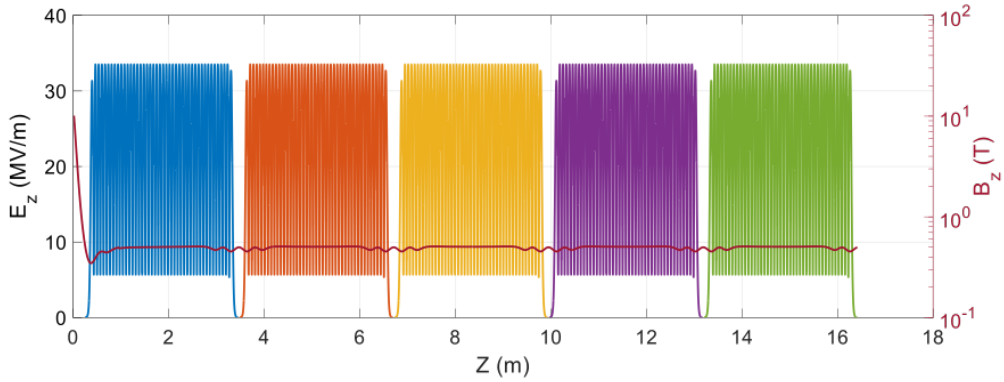

Figure 38: Electric and magnetic field profiles along the whole capture system for the the Capture System –version 0. It includes the magnetic field for the HTS solenoid together with the NC long solenoid installed around the capture linac and the electric field for 5 accelerating structures.

3.3 Optimization Studies toward Better Performance

Capture system studies are in progress to provide the optimized positron bunch 6D phase space matched to the positron linac and DR. In such a way, the first simulations have been carried out in two main domains: matching device field profile and capture system RF structure length. The investigations on the distance between the target and the first RF structure and possibility of installing the additional DC solenoid in this region are ongoing.

3.3.1 AMD field profile

To study influence of matching device field profile on positron beam performances theoretical on-axis magnetic field distribution of the AMD was used

$$B_z(z) = \frac{B_0}{1 + \alpha z} + B_{sol}, \tag{1}$$

where $B_0 = 12$ T is a maximum value of the magnetic field at the target exit surface, α is a coefficient in m^{-1} units, which defines a rate of the AMD field decay and $B_{sol} = 0.5$ T is a constant on-axis field of a DC solenoid installed along the capture linac. Figure 39a shows the field distributions for different values of α in the range from 10 m^{-1} to 60 m^{-1}.

In these studies, the positron beam parameters were evaluated at the exit of RF structure, which is installed at the fixed distance from the target (field in the accelerating structure field map starts at 0.22 m from the target). A 2 GHz TW RF structure consists of 60 cells with 9/10 π phase shift per cell (structure length is 4.3 m) has been employed. Phase and amplitude of the accelerating structure was set to get maximum energy gain of 30 MeV. Parameters of the positron beam analyzed at the RF structure exit were calculated for the distribution withing a range of $\pm$ 0.2 m from the reference particle. Figure 39 shows the results of the simulations. Bunch phase length is a phase interval,

Table 10: Results of the simulations for two different options of the AMD and two different options for the capture RF structures. The safety factor of 2 is assumed for the final positron bunch charge. The values, which correspond to the Capture System -verison 0 are marked in bold.

	Baseline AMD/FC		Alternative AMD/SC sol.		
Drive beam parameters	Value		Value		Unit
Beam energy	6		**6**		GeV
Number of bunch	2		**2**		
Bunch charge	2	2.4	**1.2**	1.7	nC
Bunch length (rms)	1		**1**		mm
Beam size (rms)	0.5		**0.5**		mm
Bunch separation	>17.5		**>17.5**		ns
Repetition rate	200		**200**		Hz
Beam power	4.8	5.8	**2.9**	4	nC
Normalized Emittance	15		**15**		mm.mrad
Energy spread (rms)	0.1		**0.1**		%
Target parameters					
Thickness	17.5 (5X0)		**17.5(5X0)**		mm
Deposited power	1.1	1.4	**0.7**	1.0	kW
PEDD	7.4	9	**4.5**	6.2	J/g
Capture linac parameters					
Frequency range	L-band	L-band	**L-band**	L-band	
Iris aperture 2a	60	40	**60**	40	mm
Accelerating gradient	20	16	**20**	16	MV/m
Solenoid strength	0.5	0.5	**0.5**	0.5	T
AMD peak magnetic field*	7 (3)	7 (3)	**15 (12)**	15 (12)	T
e+ par. at DR entrance					
Beam energy	1.54		**1.54**		GeV
Bunch charge	8		**8**		nC
Positron yield	4	3.3	**6.6**	4.8	$N_{e^+}^{Acc}/N_{e^-}$
Bunch length (rms)	3.1	2.6	**3**	2.7	mm
Normalized emittance (rms)	12.2	7.3	**13**	7.3	mm.rad
Energy spread (rms)	1.4	1	**1.6**	1.2	%

* The magnetic field at the target exit for each option is shown in between the parentheses. In case of the FC, the DC solenoid field 0f 0.5 T starts from the target location.

which contains 70% of particles in the bunch. The fast field drop in the AMD provides more shorter bunches but also leads to larger particle losses.

To study beam dynamics in more detail, a 2D scan of the RF structure phase at different values of α parameter was carried out. A normalized 5D beam brightness was used as the figure of merit taking into account bunch phase length, positron yield (bunch charge) and transverse beam emittance. Figure 40 shows the final result. The distribution has two particular peaks: the higher peak corresponds to acceleration of the tail of the initial longitudinal particle distribution and the smaller one corresponds to the acceleration of the head of the bunch. Moreover, the fast field drop of the AMD field provides higher beam brightness. It is important to note that at highest brightness

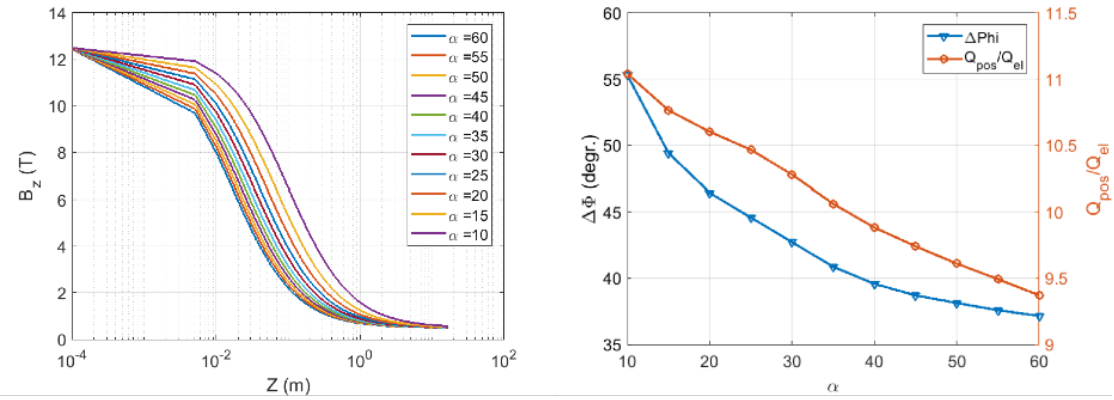

(a) (b)

Figure 39: Optimization of the AMD field profile. (a) On-axis AMD magnetic field distribution according to Equation 1. (b) Positron bunch phase length and positron yield as the function of α parameter.

99% of positrons drops in the first RF bucket.

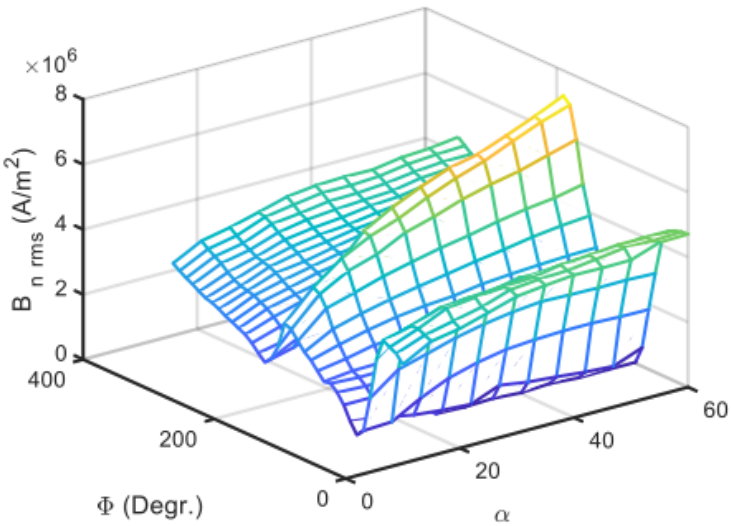

Figure 40: Optimization of the AMD field profile. Normalized beam brightness as a function of RF structure phase and AMD field decay parameter α.

3.3.2 RF structure length

Study of the RF structure length impact on the positron beam parameters was performed by changing number of structure cells in the range from 28 (2.13 m) to 74 (5.23 m). Elec-

tric field amplitude has been chosen to provide maximum energy gain of 15.95 MeV/m. The AMD field coefficient α has been chosen to be 60 m^{-1} as it corresponds to the maximum brightness (see Fig. 40 and Fig. 41a). The main results including the beam brightness, energy and positron yield are shown in Fig. 41.

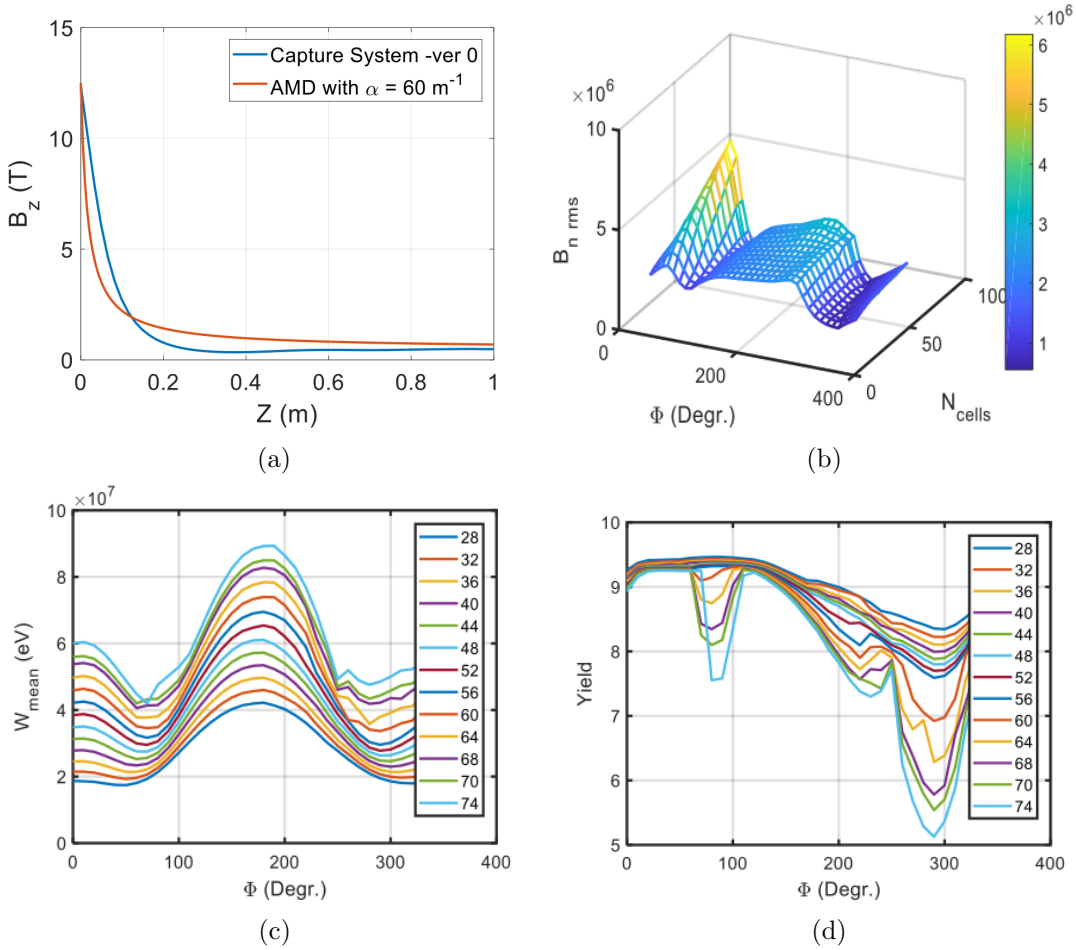

Figure 41: Optimization of the RF structure length for the positron capture section. (a) Magnetic field profile for the HTS solenoid and the theoretical AMD, which maximizes the positron beam brightness. (b) Normalized beam brightness as a function of RF structure phase and length. (c) Positron beam mean energy and (d) yield as a function of the RF structure phase shown for different values of the RF structure length.

The brightness increases with the RF structure length at the structure phase of 50°. Although this phase corresponds to the maximum positron yield, it does not maximize/minimize the mean positron energy. The positron yield decreases with the RF structure length as, probably, the structure acts as a collimator. Table 11 shows comparison of the positron beam parameters for two structures with the length of 5.23 m

and 3.21 m at the phase of 50°. The latter corresponds to the RF structure length of the Capture System -version 0. The longer structure allows for stronger bunching process resulting in a denser positron beam longitudinal distribution (see Fig. 42).

Table 11: Optimization of the RF structure length for the positron capture section. Positron beam parameters obtained by using the 5.23 m long RF structure compared to the RF structure adopted by the Capture System -version 0.

	L = 5.23 m 74 cells	L = 3.21 m 44 cells
Maximum energy gain [MeV]	83	51
Mean beam energy [MeV]	49	26
Bunch length (rms) [mm (deg.)]	8 (19°)	11.9 (29°)
Energy spread (rms) [%]	32.7	42.8
Positron total yield, N_{e^+}/N_{e^-}	9.2	9.3
Normalized emittance (rms) [mm.rad]	14	14

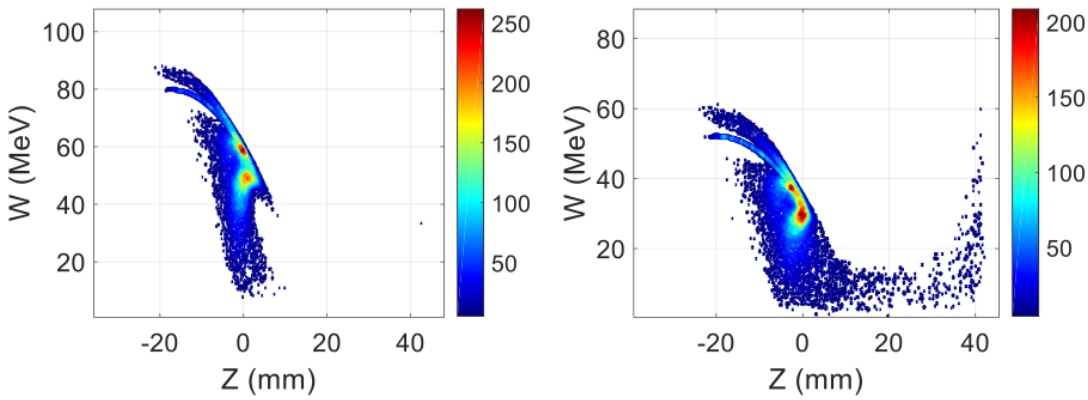

(a) (b)

Figure 42: Optimization of the RF structure length for the positron capture system. (a) Longitudinal phase space of the positrons at the end of the 5.23 m and (b) 3.21 m long RF structure.

3.4 Radiation Load Studies for SC Solenoid-based Capture System

The interaction of the electron drive beam with the positron production target gives rise to an intense flux of secondary particles. Only a fraction of the original drive beam energy contributes to the final positron yield, while most of the power is dissipated in the target, the AMD and the downstream capture linac. The resulting thermal load and cumulative radiation damage in the different components require a careful assessment in the engineering design process. This concerns in particular the design of the production target and the optimisation of absorbers, which protect sensitive components like the superconducting coils of the AMD.

In order to quantify the impact of secondary radiation fields, dedicated radiation transport studies were carried out with the FLUKA Monte Carlo code. The FLUKA geometry model is illustrated in Fig. 43. The target was modelled as a simple tungsten disk, with a length of 17.5 mm. The target was surrounded by a 1.9 cm thick tungsten shielding, which reduces the heat load and radiation damage in the AMD. The inner radius of the HTS coils of the AMD, placed in a cryostat, was 6.1 cm. A second radiation absorber (tungsten plate) was placed between the AMD and the first RF structure of the capture linac.

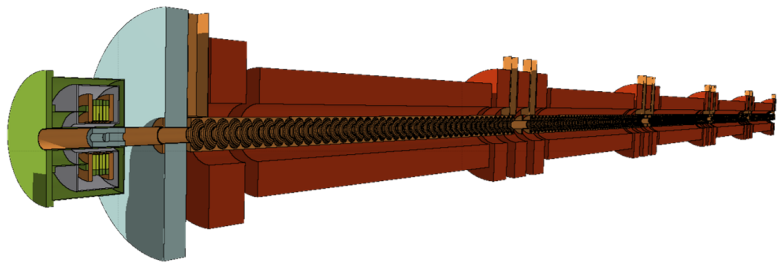

Figure 43: Side cut into the AMD and RF structure downstream.

The radiation load studies assumed a drive-beam energy of 6 GeV, a bunch charge of 3.47×10^{10} e− and a repetition frequency of 200 Hz, which results in a drive beam power of 13.43 kW. With such an electron beam, the target and surrounding shielding absorb around 3.1 kW, with a maximum power density of 80 kW/cm^3 at the downstream face (see Fig. 44). This heat load poses a significant challenge for the target design; possible engineering solutions and cooling options are presently under study. Assuming 200 days of operation per year, the radiation transport simulations show that the displacement damage in the target can reach a peak value of 8 DPA/year for FCC-ee operation at the Z-pole. Possible mitigation measures need to be elaborated, like the design of remote handling system, which enables a regular replacement of the target assembly. For the HTS coils of the AMD, a maximum of 30 mW/cm^3 power density is obtained, which is considered acceptable. The cumulative dose in the coils can reach 22 MGy/year for operation at the Z-pole. Since no organic insulation materials are used in the coils, these dose values could be acceptable, but require a further assessment. Potentially a slight increase the shielding thickness and hence the presently assumed coil aperture is needed.

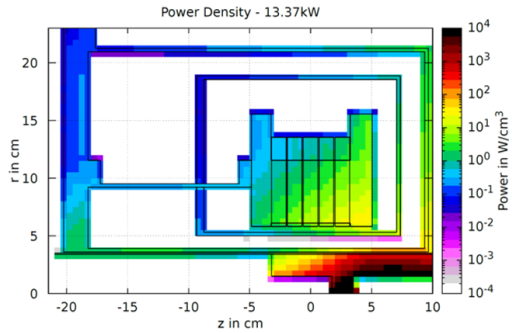

Figure 44: Power density on the AMD, averaged over the full azimuth angle. The target and the shielding are most impacted, while the coil are well protected.

For the capture linac the first out of 5 structures is the most impacted one. A tungsten shielding between the AMD and the capture linac protects especially the front face of the linac. However, the most energetic off track particles are close to the beam centre and cannot be caught with the shielding but instead they impact the capture linac inside. This leads to up to 190 W absorbed in cell 7 as the highest absorbed power (see Fig. 45). From this point, the power per cell decreases significantly to around 40 W per cell. Even the 190 W do not pose a problem, as this is close to the power of the RF structure itself. The solenoid around the RF structure is supposed to be normal conducting. This means that the maximum numbers obtained there, 2.4 mW/cm^3 for power density, 2.8 MGy/year for time integrated dose, and 1×10^{-5} DPA/year, are feasible values. The

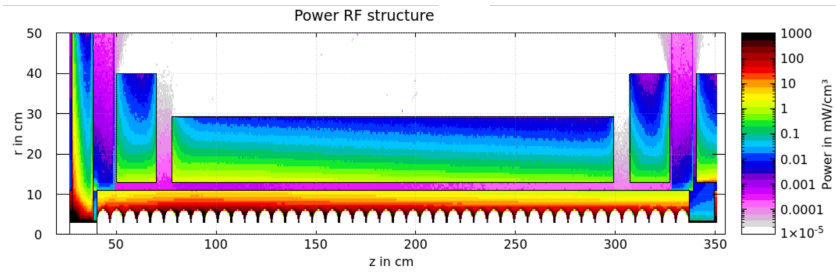

Figure 45: Power density on the first RF structure. The heat load on the cells is much higher, than on the solenoids, placed further outside and protected by the material further inside. The shielding in front, protects the face of the RF structure.

capture linac is assumed to consist of five RF structures with 44 cells, which are surrounded by solenoids. The simulations show that more than half of the power originally carried by the electron drive beam is lost in the linac, mainly in the first structure. The tungsten shielding between the AMD and the linac protects the front face of the linac, but cannot intercept the most energetic secondary particles near the beam axis, which are then lost on the linac walls. The highest radiation-induced power deposition in a single RF cell is about 190 W, but decreases to about 40 W towards the end of the RF

structure (see Fig. 45). The thermal load due to RF wall losses is estimated to reach a similar magnitude as the average radiation-induced power deposition per cell. With an adequate cooling design, the radiation load in the linac is expected to be manageable. The solenoids around the RF structure are assumed to be normal conducting. The integrated dose in the solenoids is estimated to about 3 MGy/year for operation at the Z-pole, which must be considered in the choice of materials.

3.5 Design and Integration of the FCC-ee Positron Source Target: Current Status and Challenges

The FCC-ee positron source target is the device in charge of generating particles (i.e. positrons) by colliding a high intensity primary electron beam on it, which produces gamma rays and triggers the *pair production* mechanism. At a design level, the positron target presents two main challenges: *i*) a high energy deposition density due partly to a small incident beam size and *ii*) the integration of equipment to accelerate and capture the produced positrons in a limited space. Each topic is briefly discussed below.

For the current beam parameters (2 bunches with intensity and frequency of 3.47×10^{10} e^- and 200 Hz, respectively), the resulting primary electron beam power is 13.34 kW. Out of this beam power, 3.6 kW are deposited in the target along its axis, starting in the impact zone and increasing in value along the thickness, with its peak density located near the downstream surface of the target. The power distribution occurs in a small volume fraction of the target and needs to be properly dissipated. To this end, it is required to design a cooling system capable of removing the heat from the impact zone. In addition, the resulting thermal gradient needs to be minimized as much as possible so that the generated thermal stresses are kept within the material's fatigue limits. Currently, the option of a fixed target is being explored. Figure 46 shows a diagram of the current status of the target design with its components and its location inside of the Adiabatic Matching Device (ADM). Tungsten was selected as target material due to its high melting point (3400 °C). However, it is brittle at room temperature (RT), has a medium thermal conductivity (173 W/mK at RT) and is prone to oxidation and further embrittlement at high temperature in direct contact with water. As a solution, the target is proposed to be embedded in a copper interface which presents an excellent thermal conductivity (386 W/mK at RT), following the adopted solutions in other research facilities as SuperKEKB [37] and ITER [38]. In addition, taking advantage of the state-of-the-art additive manufacturing technology, the cooling circuit would be integrated in the copper interface so that it can be located as close as possible to the target. However, for a proper heat transfer, it is required to ensure the bonding between these two dissimilar materials (W-Cu). Another consequence of the high-energy density deposition is the radiation damage, which is measured by the displacements-per-atom (DPA). This allows estimating the level of damage of a material working under a radiation environment. FLUKA simulations estimate that the target would undergo up to 8 DPA/year (although in a considerably small volume around its center). To put this in perspective, the European Spallation Source target (ESS) is expected to undergo 2.5-10 DPA during a 5-year lifetime [39, 40]. As a consequence,

a significant degradation in the material properties is expected. As an example, pure tungsten irradiated with protons and an accumulated dose of 5.8 DPA, experienced a 50.3% reduction in thermal conductivity respect to the unirradiated sample at RT [40]. Therefore, this topic needs further investigation.

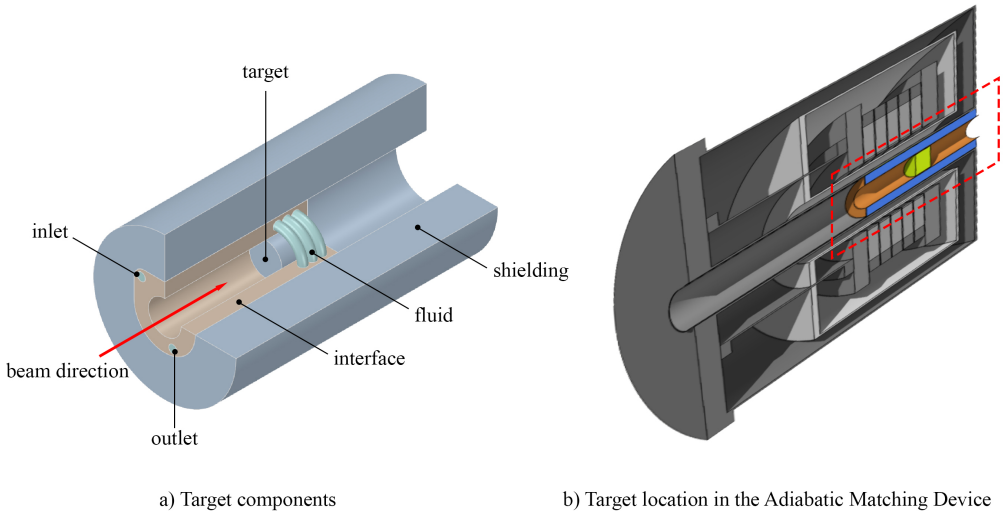

Figure 46: FCC-ee positron source target a) components description and b) location inside of the ADM

For the current target design concept have been identified and key specific items are being addressed.

Some of those aspects will be developed in combination with the PSI-P^3 target design:

- Precise positioning and alignment of the target and its associated shielding inside the beam pipe of the solenoid
- Routing of the cooling circuits inside the beam pipe
- Requirement in term of interfaces with the surrounding of the target (i.e. vacuum connections)
- Replacement of the target (for maintainability)

In addition, requirements in term of radio-protection aspects need to be assessed to define the size of the shielding around the system and its surrounding environment.

4 Damping Ring and Transfer Lines (WP4)

In the present FCC-ee pre-injector configuration, see Fig. 1, an electron beam from a low-emittance RF gun is accelerated by an S-band linac up to 6 GeV, then it is directly injected into a pre-booster Damping Ring. On the other hand, the positron beam is generated by hitting the electron beam on a positron target, then it is accelerated up to 1.54 GeV and injected in the Damping Ring for emittance cooling. A complex system of Transfer Lines is used to bring back the positron beam from the Damping Ring to the 1.54 GeV linac stage, in order to accelerate it up to 6 GeV. Transfer Lines include doglegs to implement injection and extraction in and from the Damping Ring, and arcs to bring back the cooled positron beam to the entrance of the high energy common linac stage. An Energy pre-Compressor System installed between the positron linac and the Damping Ring is used to reduce the incoming beam energy spread in order to maximize the injection efficiency as described in Par. 4.3. A bunch compressor at the entrance of the common linac is used to keep under control the rsm bunch length of the incoming positron beam.

Recently, the common linac duty cycle has been increased from 200 to 400 Hz, with two bunches per RF pulse. This new configuration imposed to revise the Damping Ring injection-extraction timing in order to account for the additional time necessary to avoid the presence of two different kinds of particles in the same common linac RF pulse. A timing revision compatible with the latest pre-injector layout is presented in Par. 4.1.3. In this context the WP4 working package is organized into four distinct tasks:

WP4.1: Damping Ring,

WP4.2: Transfer Lines to/from Damping Ring,

WP4.3: Energy pre-Compression System before Damping Ring injection,

WP4.4: Bunch length Compression before re-injection in the common linac stage.

4.1 Damping Ring overview

The purpose of the Damping Ring (DR) design is to accept the 1.54 GeV beam coming from the linac, damp the positron/electron beams, and provide the required beam characteristics for injection into the common linac (see Fig. 1). In this regard, the DR has quite challenging design requirements. DR should reduce by orders of magnitude the beam emittance in particular for the positron beams, and should provide large beam acceptance in order to catch the beam from the positron linac, which has a large distribution in the 6D phase space. The DR is about 240 m long and the energy is selected to avoid spin resonances. According to the current design, a FODO-type cell is chosen, the DR is made up of two arcs and two straight sections housing the damping wiggler magnets, RF cavity, and injection/extraction equipment. The injection will be done by using an on-axis scheme. The DR beam structure foreseen a sequence of a maximum of 9 bunch trains, each of them including two bunches. Single bunch current is planned to reach a rather high intensity as it varies in the range of $0.6 \div 5.7$ mA. The injected

beam must reach the nominal equilibrium emittance of 0.96 nm in a store time of about 40 msec. High currents stored in rather short bunches, see Par. 4.1.2, require a careful evaluation of beam lifetime and a comprehensive analysis of collective effects taking into account a realistic impedance budget, and considering beam coupling with the RF system. Preliminary analytical estimations [25] of various collective effects such as space charge (SC), intra-beam scattering (IBS), longitudinal micro-wave instability, transverse mode coupling instability (TMCI), ion effects, electron cloud and coherent synchrotron radiation (CSR), have been performed for an intermediate version of the DR optics. No major limitations are expected from IBS, TMCI and CSR. Concerning the SC, the tune shift at the equilibrium state might be an issue. Furthermore, the Boussard criterion is below the longitudinal impedance assuming a vacuum chamber radius of 10 mm. It was shown that the neutralization density exceeds the e-cloud instability threshold for the equilibrium state. The fast rise times of the fast ion instability can be compensated with a feedback system, provided a vacuum pressure of 10^{-9} mbar is achieved in the DR. Similar study must be repeated for the latest DR optics and considering a realistic model for the beam pipe and vacuum equipment. DR also requires a purpose designed injection/extraction timing system in order to assure the proper ring filling, the required stored time for damping, and the necessary delay in the train extraction that guarantees to have only one kind of particle in a given RF pulse of the common linac.

4.1.1 Dynamic aperture

The Dynamic Aperture (DA) has been evaluated using the PTC [27] module of MAD-X [7] using two different approaches:

quick: the tracking has been performed starting in the transverse plane on a random position within a box of 4x4 cm^2. The particles have been tracked up the 2000 turns without radiation damping. The initial energy deviation has been considered up to 5%. In Fig. 47-left the result of this tracking is shown. At the nominal energy in both planes, the stable region, normalized as a function of beam width, is of the order of three $\sigma_{h,v} = \sqrt{\beta_{h,v}\epsilon_{h,v} + (D_{h,v}\delta_E)^2} \simeq 3mm$.

full: tracking performed using the CDR [2] nominal 6D beam envelope at the injection with radiation damping enabled. Positrons have been tracked for 10000 turns, corresponding to a store time equal to the damping time in the DR. The injected beam emittance in the transverse planes is assumed to have the CDR nominal parameters: $\epsilon^{geo}_{h,v} = 1.29$,1.22 mm mrad, , respectively for horizontal and vertical and $\delta_E \simeq 5\%$ for the energy spread. The result is shown in Fig. 47-right.

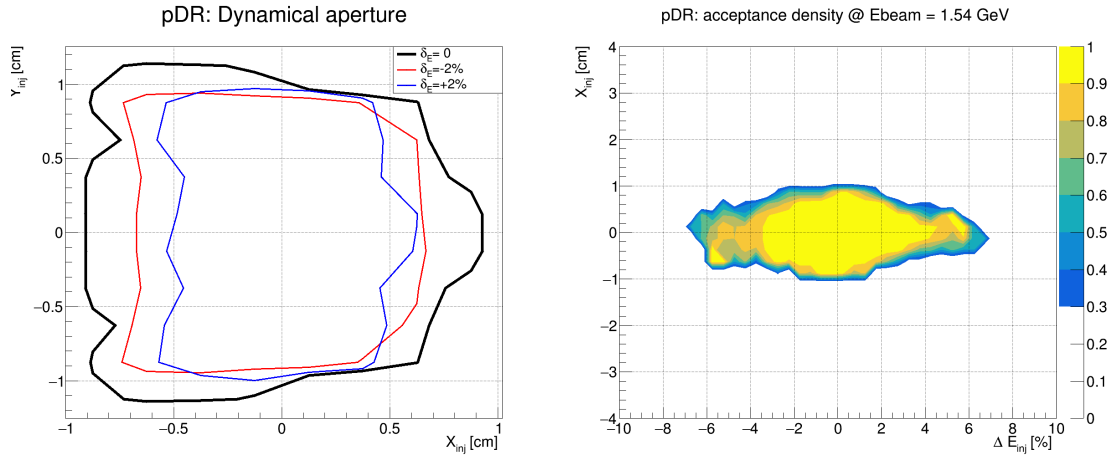

Figure 47: Dynamic aperture. In the left plot, the transverse stable region is shown for the nominal beam energy (1.54 GeV - black) and for ±2% energy relative deviation (blue and red, respectively). While the stable region is kept quite constant within 2% energy spread is observed to drop significantly for higher deviations. In the right plot, the result of the *full* simulation is reported. The color map represents the fraction of survived particles at the end of the tracking as a function of the initial horizontal position and energy deviation. The survival probability includes the full 6D particle phase space treatment. The beam is assumed to be Gaussian distributed with CDR nominal widths in the transverse plane.

With the current DR lattice and the CDR [2] incoming beam parameters, the DR acceptance is estimated to be $\epsilon_{ACC} \simeq 47\%$ thus implying a factor of two of reduction in the positron yield without using of the Energy Compressor described in Par. 4.3.

4.1.2 Longitudinal beam dynamics

The Radio Frequency (RF) cavity is fundamental to define the DR longitudinal beam dynamics. The RF cavity must: restore the energy lost from the beam by incoherent Synchrotron Radiation emission U_0, provide longitudinal beam parameters compatible with stable beam dynamics conditions and, what is more important in this specific case, provide a large energy acceptance compliant with the large energy spread of the incoming positron beam. In the following considerations we assume to use as RF cavity the LHC type SC device operating at the frequency of 400 MHz, as already proposed in the CDR [28]. This cavity consists of two RF modules housed in the same cryostat. It is worth reminding, that in the following we will indicate as RF voltage the total voltage of the two RF modules.

In principle to accept a 6% incoming beam energy spread a RF voltage of V_{RF}= 8 MV is required. In Tab.12 is reported a summary of the beam dynamics parameters computed for several RF voltages and considering momentum compaction, α_c = 0.001535, and

harmonic number, h = 319. The listed parameters are calculated for stationary bunches at the equilibrium, and in the zero-current approximation. In order to get more realistic quantities, it is necessary to perform comprehensive numerical simulations taking into account the number of circulating particles, the ring impedance, how the beam couple with the ring impedance, RF beam loading, and RF transient beam loading.

In the present DR configuration high RF voltage determines rather short bunch length values, which can represent an issue for beam lifetime and for several collective effects. This aspect together with the result obtained from tracking studies about transverse beam acceptance led us to fix V_{RF} = 4 MV as a reference value for the RF cavity voltage.

V_{RF}	8 MV	6 MV	4 MV	2 MV
U_0 [keV]	227.1			
DE/E_s	0.71×10^{-3}			
Ω_S [kHz]	25.13	21.918	17.888	12.618
T_0 [μs]	0.79801			
ω_0 [s^{-1}rad]	7.87×10^6			
ν_s	0.003215	0.00278	0.002272	0.0016
L_{bunch} [mm]	2.07	2.39	2.93	4.15
ϕ_S [rad]	0.0283967	0.0378663	0.0568164	0.113817
$E - E_S$ [GeV]	0.124	0.107	0.0862	0.058
$\Delta\phi$ [π]	1.8	1.7769	1.7269	1.6016
L_{bucket} [m]	0.6788	0.6664	0.6476	0.6006

Table 12: Longitudinal beam dynamics parameters

A preliminary estimate of the total RF power requirement, P_{RF}, can be done using the following simplified formulas:

$$P_{RF} = P_b + P_l \tag{2}$$

where P_b accounts for the power necessary to restore the incoherent synchrotron radiation emission, and P_l for the cavity wall dissipation. These quantities are given by:

$$P_b = I_b \Delta U_0 / e \qquad P_l = V_{RF}^2 / 2 n_{RF} R_{shunt} \tag{3}$$

In Tab. 13 are reported the preliminary P_b values computed using the aforementioned numbers about beam currents, and DR bunch filling scheme.

Positron charge from linac[nC]	I_b[mA]	I_{tot}[mA] nb=2÷18	P_B[KW]
4.5	5.638	11.3÷101.5	2.6÷23
0.5	0.6	1.3÷11.3	0.285÷2.56

Table 13: Power requirements

4.1.3 Injection/Extraction timing

During the positron filling, the common linac is operated at an effective repetition rate of 400 Hz obtained as the overlap between alternate 200 Hz repetition rates for electron and positron, respectively. The positron bunches (two per pulse) are produced at the source synchronized with the electron timing while the extracted ones from the DR have to be synchronized with the positron accelerating pulses of the common linac. This requirement together with the cooling time needed to reach the proper beam parameters at the extraction fully defines the timing scheme of the DR. To reach the target values of the emittance at the extraction a minimum stored time of 40 ms is needed (four damping times) while to slide from the time series of the electron pulses to the one for the positrons in the common linac, an additional store time of 2.5 ms is required. Such a delay can be accommodated only if a minimum number of nine linac pulses are stored in the DR. The timing of the primary electron pulses has to be properly scaled according to the following relation:

$$T_{gun}(i) = iT_{Rep} + \Delta_b T_{RF}(i\%N_p) \qquad i \in [0, n] \tag{4}$$

where T_{Rep} is the period of the injection pulse rate (200Hz), Δ_b is the time differences between the first filled buckets in the DR for each pulse[3], T_{RF} is the radiofrequency of the DR (400 MHz) and N_p is the number of stored pulses in the DR (9 minimum). As shown in the Eq. 4, the effective time of the electron pulses has to be adjusted within the range of the synchrotron period (T_S $1\mu s$). Analogously the extraction time has to follow this relation:

$$T_{Ext}(i) = T_{gun}(i) + \Delta T_{DR} + T_S/2 + T_{Rep}/2 - \Delta T_{12} \tag{5}$$

where ΔT_{DR} is the minimum store time, $T_S/2$ takes into account the DR half turn between the injection and extraction section, $T_{Rep}/2$ takes into account the extra time to slide from electron to positron common linac timing and ΔT_{12} represent a fixed phase adjustment that takes into account the propagation time from DR to the entrance in the common linac. The Eq. 5 shows that it is possible to adjust the extraction timing only in units of the synchrotron period.

4.1.4 DR Layout upgrades

In parallel to the current DR design based on the CDR of the FCC project, a new DR layout study has also been started [2, 26]. The reasons driving the new design can be summarized as follows: reduce the number of magnetic elements and increase the dipole strength while keeping normal conducting device, optimize the FODO cell phase advance for minimum beam equilibrium emittance and increase the number of straight

[3]Since linac pulses contain two bunches, the effective time structure of filled buckets in the DR depends not only by the number of stored pulses but also from the arrival time difference between the two bunch in the same pulse. Currently, this time difference is set at 25 ns because of the main ring requirements.

sections in order to have independent sections for RF cavity, damping wigglers, and injection-extraction.

The new approach to DR design makes the damping time shorter, which meets some new recent requirements. Reducing the dipole magnet number also determines a considerable reduction of the number of other magnets (sextupole, corrector, ...), and beam diagnostics. The optimum phase advance of the FODO cell ($\simeq$ 135degree) is chosen for minimum emittance. In addition, three straight sections are planned for the layout upgrade. Besides, a combination of damping wiggler magnet and Robinson wiggler magnet is also used to meet the design requirements. These wiggler magnets provide smaller emittance, and shorter damping time while causing a rise in energy spread and energy loss per turn. This requires a comprehensive analysis to achieve the optimal trade-off among all the different parameters. The preliminary results showed that it is possible to reach around 4.9 nm.rad horizontal geometrical emittance, 6 ms horizontal damping time in around 257 m circumference as allocating 18 bunches. In this first design, 72 dipole magnets, 18 m long damping wiggler magnets (2 T), and 3.8 m long Robinson wiggler magnets (1.2 T) are used. The energy loss per turn is 0.253 MeV, energy spread is 0.14%.

4.2 Transfer Lines overview

The design of the FCC-ee pre-injector Transfer Lines (TL) is inspired by criteria of high modularity, suitable to deal with a project in constant evolution, and, as a consequence, requiring frequent modifications.

The latest layout of the FCC-ee pre-injector complex is presented in Fig. 1. The recent decision to use the DR for the positron beam only, largely simplified the TL layout allowing to drop the line dedicated to the electron beam and reducing the complexity of the DR injection-extraction branches. However, the optics for the electron beam TL, including a long 180 degrees arc turning around the DR had been designed in detail, and some preliminary studies to evaluate a possible contribution of the CSR to the beam emittance dilution had been performed by using the ELEGANT [6] simulation code. Presently the positron beam TL includes a line driving the positron beam from the linac To the DR injection section ($pTLi$), and an extraction line bringing the damped beam back to the high energy common linac ($pTLe$). The $pTLi$ is very demanding in terms of beam transport efficiency as the beam from the linac features rather broad distributions both in the transverse and in the longitudinal phase space. To improve positron beam injection efficiency in the DR an Energy Compression System (ECS Par. 4.3) has been added just after the positron linac.

The $pTLe$ is based on a combination of periodical straight section modules, implemented by a FODO magnetic structure, and arcs built by combining basic cells providing 30 degrees of deflection each.

4.2.1 Positron extraction line

The arcs in the *pTLe* are periodic structures based on isomagnetic triple bend cells (TBA) whose parameters and elements are listed in Tab. 14. The bends are rectangular magnets providing 10 degrees deflection angle each, but having asymmetric lengths, with the central being the shorter one. Each cell is achromat, isochronous, has moderate betatron oscillation amplitude both in the horizontal and in the vertical plane, and moderate maximum horizontal dispersion excursion, $|\eta_x| < 0.3$ m. The cell also features very low $\mathcal{H}$ function values suitable to avoid possible beam quality degradation induced by CSR emission.

parameter[units]	value	quadrupole gradient[m^{-}2]
θ_b [rad]	0.1745	$K_{D01} = K_{D04} = -9.84$
L_b [m]	1.506/0.865	$K_{DD2} = K_{D03} = -1.905$
ρ [m]	8.633/4.959	$K_{F01} = K_{F04} = 7.281$
n_{QUAs}	8	$K_{F02} = K_{F03}$=4.623
n_{SXTs}	2	sextupole gradient[m^{-}3]
L_{quads} [m]	0.2	K^S_{D01}=K^S_{D02}=-58.738
L_{cell} [m]	16.2573	K^S_{F01}=K^S_{F02}=44.294

Table 14: TBA cell parameters.

The evolution of the beta functions and of the horizontal dispersion is reported in the Fig. 48.

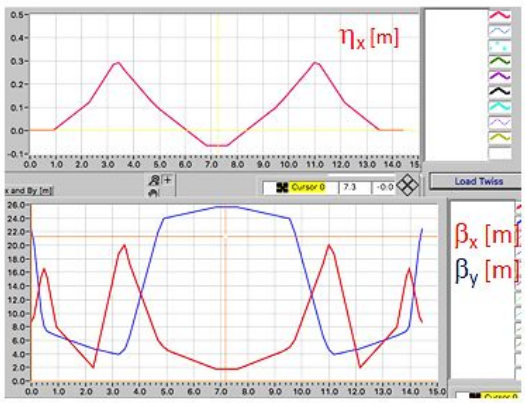

Figure 48: Evolution of the betatron oscillation and horizontal dispersion function in the *pTLe* TBA cell.

4.3 Energy Compressor section

Preliminary studies of the dynamic aperture of the positron DR show that the stability region shrinks to almost the incoming beam size as the relative energy variation exceeds

2%. The energy spectrum RMS of the incoming positron beam is 8% and only 36% lies within 2% of the nominal energy. The energy distribution can be compressed using an element with a non-null R_{56} and a RF cavity tuned on the zero crossing. In the first part of the ECS, the bunch length of the beam is increased according to the momentum spread, and a linear correlation is established between the energy and the longitudinal position along the bunch. Finally, in the second part of ECS, conveniently phasing the cavity at zero crossing, it is possible to compensate for the energy deviation while preserving the mean momentum of the bunch. The final effect of the ECS on the beam is a reduction of the total energy spread and a corresponding increase in the bunch length. A slice analysis of the positron energy distribution coming from the linac shows a predominant uncorrelated energy spread. Both negative and positive R_{56} can be used. The first option considered is a C-shape chicane. It consists of four rectangular bending dipoles. This chicane brings the beam through a by-pass transport line and then returns it to the linac axis, it provides a closed dispersion due to geometrical symmetry without using any quadrupole. In the first-order approximation, the chicane modifies the longitudinal position of each electron in the bunch according to the following equation:

$$s(f) = s(i) + R_{56} \cdot (E(i) - E_{mean})/E_{mean} \tag{6}$$

The energy of each particle is modified according to the RF relative phase:

$$E(f) = E(i) + V \cdot (\cos(s(i) \cdot k + \phi_o)) \tag{7}$$

where $k = 2\pi/\lambda_{RF}$ and λ_{RF} is the RF wavelength. Applying this transformation it is possible to model the action of the ECS analytically.

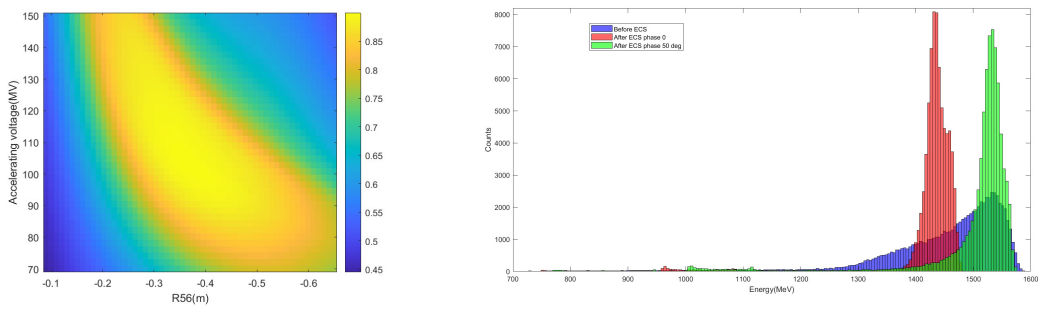

Figure 49: Left: fraction of particles with energy in the range ±2% from the peak of the energy distribution vs chicane R_{56} and RF voltage. Right: the energy distribution before (blue) and after (red/green) the ECS. The zero crossing in the cavity shifts the peak energy (red), which could be recovered by properly phasing the RF cavity (green).

The map in Fig.49-left shows the fraction of particles within a ±2% deviation from the peak of the energy distribution as a function of R_{56}, and the accelerating voltage (AV) of the cavity. The beam energy distribution obtained with the analytical transformation

shows some difference with respect to the tracking with ELEGANT that will be used as a reference for the start-to-end simulation. It is clear that $AV > 80$MV, and $|R_{56}| > 0.22$ m are needed to have a fraction of the beam higher than 85% in the desired energy range. The ECS uses the same type of cavity foreseen for the positron linac working at the frequency of 2GHz and optimized to handle the big transverse dimensions of the beam. Two cavities of this type can provide an accelerating voltage slightly higher than 120 MV. A R_{56} = -0.25 m is achieved by using four dipoles (1 m long , 1.34 T filed intensity, 15.2^o deflection), separated by 1 m drifts. This chicane together with the proper RF cavity setup (120 MV) has been used for the ECS simulation with ELEGANT, as shown in Fig. 49-right. The compression of the energy distribution is evident. The zero crossing in the cavity shifts the peak energy (red histogram). It could be recovered by properly phasing the RF cavity (green histogram) or increasing the linac energy correspondingly. The fraction of particles within the range of $\pm 2\%$ of the peak energy with aforementioned ECS parameters results to be 86%. The inclusion in the simulations of CSR according to the 1D model used by ELEGANT [29] doesn't show relevant effects on the transverse emittance and the energy spread.

5 PSI Positron Production (P^3) Project (WP6)

The P^3 experiment [30] constitutes the WP6 of the collaboration as a demonstrator for the positron (e+) source. The goal of WP6 is to design and install such demonstrator in the SwissFEL facility, and validate through an experiment a range of novel techniques that, according to simulations, have proven potential to increase the e+ yield by one order of magnitude with respect to the state of the art. This chapter overviews the current status of the main components and provides a summary of the main progress over the last year, particularly regarding beam dynamics and beam diagnostics.

5.1 Component Overview

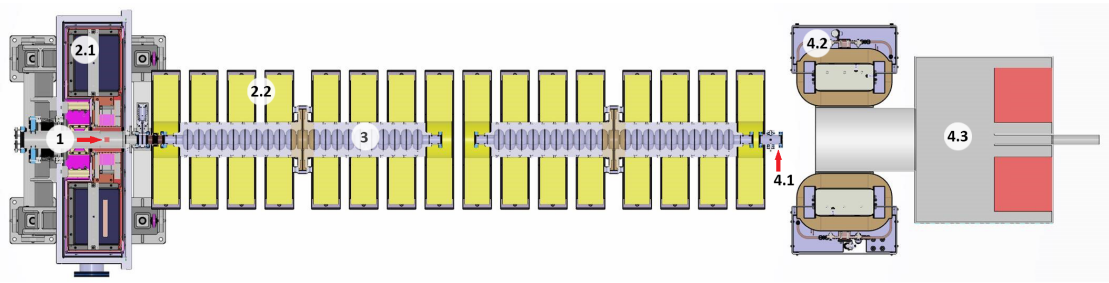

Figure 50: Section view of P^3 layout. Numbering next to components corresponds to first and second columns of Tab. 15.

Figure 50 shows the latest design status of the P^3 components. These components fulfill a wide range of purposes, and their design status highly advanced in some cases. A more detailed overview of them is presented in Tab. 15.

5.2 Beam Dynamics

5.2.1 Impact of Normal Conducting Solenoids

The field strength of the solenoids around RF structures has a high impact on the e+ capture efficiency [23]. A previous layout of P^3 contemplated the use of superconducting solenoids delivering a multi-Tesla field as baseline. However, for cost and manpower reasons, normal conducting, copper solenoids have been adopted. An arrangement of 8 solenoids per cavity, shown in Fig. 50, can deliver a reasonably constant field of 0.4 T. An updated simulation of the e+e- beam with normal conducting solenoids is shown in Fig. 51.

5.2.2 Study of Targets of Conical Geometry

The baseline for the P^3 and FCC-ee targets foresees the use of a 17.5 mm thick target [32], with both the entrance and exit faces flat and perpendicular to the beam motion. As a first approach to a target geometry optimization, several cylindrical and conical

Table 15: Overview of main P^3 components and their development status.

Components	Description	Status[1]
1. Target	A Tungsten (W) converter target and a 6 GeV electron (e-) drive beam from the SwissFEL linac will for e+ production.	Geometry (See Par. 5.2.2.) and mechanical support of target to be defined.
2. Magnet System	2.1. High-temperature superconducting (HTS) solenoid: peak-field of 12.7 T around the target for adiabatic emittance matching [23].	HTS tape purchased. Cryostat mechanical design highly advanced.
	2.2. Normal conducting solenoids around RF structures: constant field of 0.4 T	Layout and solenoid working point defined, magnet engineering in progress.
3. RF Cavities	Two standing wave, S-band cavities. Feeding through one central waveguide providing gradient of 18 MV/m.	Cups currently in fabrication externally. Delivery and in-house brazing during 2023.
4. Diagnostics	4.1. Arrangement of four broadband pick-ups for time structure measurement. Based on [31].	RF design defined. Mechanical design in advanced stage. Feedthroughs purchased and measured.
	4.2. Spectrometer: constant field of 0.4 T	Layout and solenoid working point defined, magnet engineering in progress.
	4.3. Vacuum chamber including Two faraday cups for e+ and e- and scintillating fiber for reconstruction of e+ energy spectrum.	Dimensions of chamber and faraday cups to be optimized. Scintillating fiber to be calibrated.

[1]The colors in the Status column represent the design development level: green = purchase phase, yellow = main task in progress, red = concept design.

geometries have been studied through Geant4 [33] and ASTRA [34] simulations. Preliminary results show potential to increase the e+ yield at the target and the damping ring by 40% and 50% respectively. Although this study is so far focused on the P^3 target, where no cooling is needed, it is to be determined if conical targets are mechanically feasible in the FCC-ee environment, subject to high-current and high-repetition rate e-beams.

5.3 Beam Diagnostics

5.3.1 Broadband Pick-Ups

Figure 52 (see also 4.1 in Fig. 50) shows an arrangement of four broadband pick-ups (BBPs) placed after the second RF cavity measure the time structure of the e+e- beam, differentiating consecutive electron and positron bunches. This tool is based on the *Fast-BPM* developed at SuperKEKB [31]. In the case of P^3, the e+ and e- bunches have a length around 30 ps, 167 ps apart from each other (half RF period). This detection requires a high-bandwith frequency response, and thus two sets of feedthroughs with cutoff frequencies at 27 GHz [35] and 65 GHz [36] have been acquired and measured.

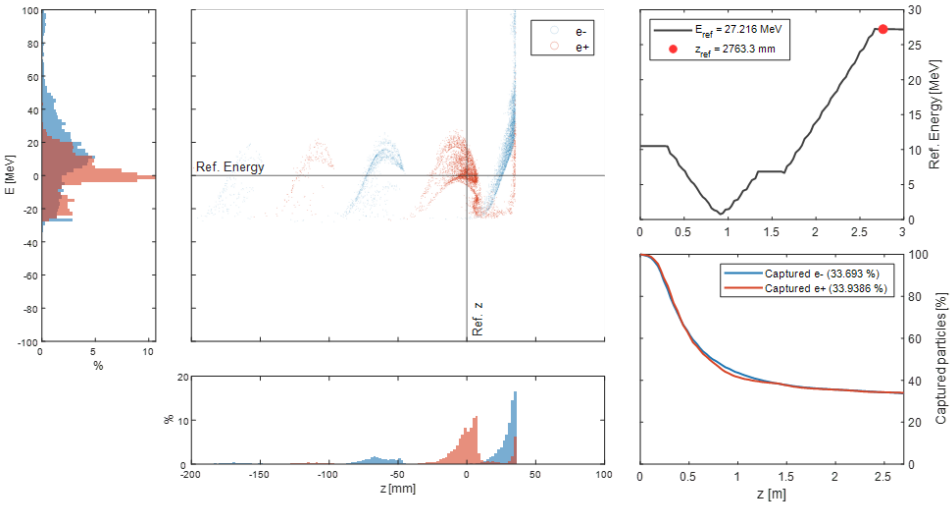

Figure 51: Simulated e+e- beam after the P^3 RF Cavities surrounded by normal conducting solenoids.

The pick-up design consists of a conical antenna in order to maximize the acquired signal amplitude and minimize possible noise sources. Figure 52 also shows the simulated response of the pick-ups over a gaussian e+ bunch of 1 nC and 32 ps long. As expected, the pick-ups act as a differentiator of the gaussian wake voltage signal.

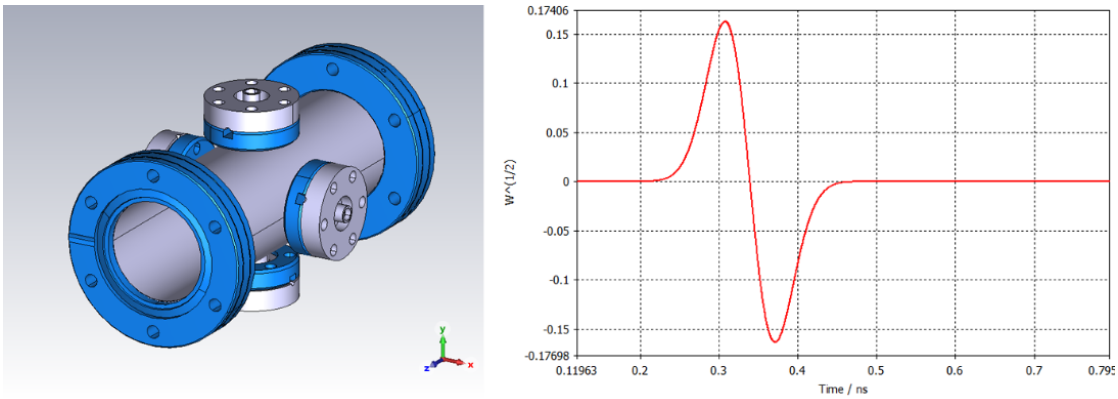

Figure 52: 3D model of the BBPs (left) and frequency response [$W^{1/2}$] over time [ns] (right).

5.3.2 Vacuum Chamber after Spectrometer

The secondary e- and e+ will be separated by a spectrometer (see 4.2 in Fig. 50) and dumped into independent Faraday cups (see 4.3 in Fig. 50) that will provide a charge

measurement integrated over many bunches. In pursuit of a compact design, these faraday cups are implemented through a 25 Ω coaxial layout, matched to the standard 50 Ω through two parallel coaxial guides. Due to the significant losses in the spectrometer walls and the rather small size of the faraday cups, only 68% and 65% of captured positrons and electrons are eventually measured.

In addition, The spectrum of the longitudinal momentum (p_z) of the beam can be measured through varying the spectrometer field strength and placing a screen of narrow width within the vacuum chamber (Not included in Fig. 50). The obtained distribution of measurements can be transformed into a histogram of p_z by applying the magnetic rigidity law. Preliminary simulations show an accurate reconstruction of the p_z spectrum through a scan up to 0.3 T of the dipole field.

5.4 Installation and Timeline

As mentioned above, the SwissFEL linac at PSI will host the experiment. Preliminary installation works of the transfer line from the SwissFEL linac to the experiment bunker have already started and will normally continue to take place during most SwissFEL shutdowns. According to a preliminary timeline, construction of the P^3 bunker and installation of components are expected to initiate in late-2024 and the experiment is to take place in 2025.

References

[1] P. Craievich, M. Schaer, N. Vallis, R. Zennaro et al., *FCC-ee Injector Study and P^3 Project at PSI*, CHART Scientific Report 2021.

[2] A. Abada, M. Abbrescia, S. S. AbdusSalam. et al. *FCC-ee: The Lepton Collider.*, Eur. Phys. J. Spec. Top. 228, 261–623 (2019), `doi.org/10.1140/epjst/e2019-900045-4`.

[3] F. Bordry, M. Benedikt, O. Bruning, J. Jowett, L. Rossi, D. Schulte, S. Stapnes, F. Zimmermann, *Machine Parameters and Projected Luminosity Performance of Proposed Future Colliders at CERN*, CERN-ACC-2018-0037, `doi.org/10.48550/arXiv.1810.13022`.

[4] N. Iida *et al.*, *Commissioning of Positron Damping Ring and the Beam Transport for SuperKEKB*, in Proc. 62nd ICFA ABDW on High Luminosity Circular e^+e^- Colliders (eeFACT'18), Hong Kong, China, 24-27 September 2018, TUPAB07.

[5] T. Brezina, *Electron source and pre-injector design for the FCC-ee*, Bachelor's Thesis, Masaryk University, Faculty of Science, Brno, Czech Republic, 2022, `doi.org/10.5281/zenodo.6922020`.

[6] M. Borland, "elegant: A Flexible SDDS-Compliant Code for Accelerator Simulation," Advanced Photon Source LS-287, September 2000.

[7] Deniau, L., Grote, H., Roy, G., Schmidt, F. (2022). *The MAD-X Program: User's Reference Manual (v.5.08.01)*. CERN ADS.

[8] A. Latina, *RF-Track Reference Manual*, CERN, Geneva, Switzerland, June 2020, DOI: 10.5281/zenodo.3887085.

[9] D. Schulte, "Placet : A program to simulate drive beams", CERN-PS-2000-028-AE and CERN-PS-2000-028-AE.

[10] A. Grudiev, S. Calatroni and W. Wuensch, *New local field quantity describing the high gradient limit of accelerating structures*, Phys. Rev. ST Accel. Beams, Vol. 12, issue 10, pages 102001, 2009.

[11] H. W. Pommerenke et al., *RF design of traveling-wave accelerating structures for the FCCee injector complex*, THPOJO08, LINAC22, Liverpool, UK, 2022.

[12] I. Chaikovska *et al.*, *Positron sources: from conventional to advanced accelerator concepts-based colliders*, Journal of Instrumentation, vol. 17, no. 05, pp. P05015, 2022.

[13] J. E. Clendenin, *High-Yield Positron Systems for Linear Colliders*, in Proc. 13th Particle Accelerator Conf. (PAC'89), Chicago, IL, USA, Mar. 1989, pp. 1107–1112.

[14] J. Sheppard, *Conventional Positron Target for a Tesla Formatted Beam*, SLAC-TN-03-072, LCC-0133, Nov. 2003.

[15] R. Chehab, F. Couchot, AR. Nyaiesh, F. Richard, X. Artru, *Study of a positron source generated by photons from ultrarelativistic channeled particles*, in Proc. of the 1989 IEEE Particle Accelerator Conf., 'Accelerator Science and Technology, 1989, pp. 283–285.

[16] R. Chehab *et al.*, *Experimental study of a crystal positron source*, Phys. Lett. B, vol. 525, no. 1-2, p. 41–48, 2002.

[17] X. Artru *et al.*, *Summary of experimental studies, at CERN, on a positron source using crystal effects*, Nucl. Instr. Meth. B, vol. 240, no. 3, pp. 762–776, 2005.

[18] T. Suwada *et al.*, *Measurement of positron production efficiency from a tungsten monocrystalline target using 4-and 8-GeV electrons*, Phys. Lett. E, vol. 67, no. 1, p. 016502, 2003.

[19] M. Satoh *et al.*, *Experimental study of positron production from silicon and diamond crystals by 8-GeV channeling electrons*, Nucl. Instr. Meth. B, vol. 227, no. 1-2, pp. 3–10, 2005.

[20] X. Artru *et al.*, *Polarized and unpolarized positron sources for electron–positron colliders*, Nucl. Instr. Meth. B, vol. 266, no. 17, pp. 3868–3875, 2008.

[21] L. Bandiera *et al.*, *Crystal-based pair production for a lepton collider positron source*, The European Physical Journal C, vol. 82, no. 08, pp. 699, 2022.

[22] A. I. Sytov, V. V. Tikhomirov, and L. Bandiera, *Simulation code for modeling of coherent effects of radiation generation in oriented crystals.* Phys. Rev. Accel. Beams, 22:064601, Jun 2019.

[23] R. Chehab, *Positron Sources*, in CAS: 5th General Accelerator Physics Course, Jyvaskyla, Finland, 1992, pp.643-678.

[24] Y. Enomoto et al., *A New Flux Concentrator Made of Cu Alloy for the SuperKEKB Positron Source*, in Int. Particle Acc. Conf 2021. (WEPAB144), Campinas, SP, Brazil, pp. 2954–2956.

[25] O. Etisken, F. Antoniou, A. De Santis, C. Milardi, F. Zimmermann, *Collective Effects Estimates for the Damping Ring Design of the FCC-ee.* IPAC2022, 2435–2438, `http://dx.doi.org/10.18429/JACoW-IPAC2022-THPOST003`.

[26] O. Etisken, C. Milardi, *Considerations about new damping ring layout*, in FCC-ee injector studies mini-workshop, November 2022, Paris, France.

[27] E. Forest, F. Schmindt, E. McIntosh, *Introduction to the Polymorphic Tracking Code*, Technical Report KEK-Report 2002-3.

[28] D. Boussard and T. Linnecar, *The LHC superconducting RF system*, LHC Project Report, 316, 1999.

[29] M. Borland, *Modeling of the micro-bunching instability*, Phys. Rev. Accel. Beams, 11, 030701(8), 2008.

[30] N. Vallis *et al.*, *The PSI Positron Production Project*, in Proc. LINAC'22, Liverpool, UK, Aug.-Sep. 2022, pp. 577-580, TUPORI16.

[31] T. Suwada et al., *First simultaneous detection of electron and positron bunches at the positron capture section of the SuperKEKB factory*, Sci. Rep. 11, 12751 (2021).

[32] I. Chaikovska et al., *Positron Source for FCC-ee*, in 10th Int. Particle Acc. Conf., Melbourne, Australia, pp. 424-427.

[33] *Geant4: A simulation toolkit. Book for application developers*, v. 11.0, CERN, Geneva, 2011.

[34] *A space charge tracking algorithm*, v. 3.2, DESY, Hamburg, 2017.

[35] Allectra GmbH, "27GHz SMA feedthrough for UHV applications." Data Sheet 242-SMAD27G, 2019.

[36] Allectra GmbH, "Microwave 1.85 mm (SMA) feedthrough." Data Sheet 242-SMAD65G, 2022.

[37] Y. Enomoto, Y. Morikawa, and M. Fukada, "Positron source and positron production target (in japanese)," *Particle Accelerator Society of Japan*, vol. 18, no. 4, pp. 269–280, 2022.

[38] T. Hirai and G. Pintsuk, "Thermo-mechanical calculations on operation temperature limits of tungsten as plasma facing material," *Fusion Engineering and Design*, vol. 82, no. 4, pp. 389–393, 2007.

[39] A. Aguilar, F. Sordo, T. Mora, L. Mena, M. Mancisidor, J. Aguilar, G. Bakedano, I. Herranz, P. Luna, M. Magan, R. Vivanco, F. Jimenez-Villacorta, K. Sjogreen, U. Oden, J. Perlado, J. Martinez, and F. Bermejo, "Design specification for the european spallation source neutron generating target element," *Nuclear Instruments and Methods in Physics Research Section A: Accelerators, Spectrometers, Detectors and Associated Equipment*, vol. 856, pp. 99–108, 2017.

[40] J. Habainy, Y. Dai, Y. Lee, and S. Iyengar, "Thermal diffusivity of tungsten irradiated with protons up to 5.8 dpa," *Journal of Nuclear Materials*, vol. 509, pp. 152–157, 2018.

Publications and Conference Contributions

- T. Brezina, *Electron source and pre-injector design for the FCC-ee*, Bachelor's Thesis, Masaryk University, Faculty of Science, Brno, Czech Republic, 2022, doi.org/10.5281/zenodo.6922020

- IPAC 2022 (12.6-17.7.2022): https://www.ipac22.org/
  - B. Humann et al., Radiation Load Studies for the FCC-ee Positron Source with a Superconducting Matching Device, https://accelconf.web.cern.ch/ipac2022/papers/thpotk048.pdf
  - P. Craievich et al., FCCee Pre-Injector Complex, https://accelconf.web.cern.ch/ipac2022/papers/wepopt063.pdf
  - S. Ogur et al., Target Studies for the FCC-ee Positron Source, https://accelconf.web.cern.ch/ipac2022/papers/wepopt054.pdf
  - Y. Zhao et al., Optimisation of the FCC-ee Positron Source Using a HTS Solenoid Matching Device, https://accelconf.web.cern.ch/ipac2022/papers/wepopt062.pdf
  - O. Etisken et al., Collective Effects Estimates for the Current Damping Ring Design of the FCC-e+e-, https://accelconf.web.cern.ch/ipac2022/papers/thpost003.pdf

- 65th ICFA Advanced Beam Dynamics Workshop on High Luminosity Circular e+e- Colliders (eeFACT2022), Sep 12–16, 2022, INFN Frascati National Laboratories, several contributions, https://agenda.infn.it/event/21199/

- Linac conference 2022 (28.08-02.09) https://linac2022.org/
  - H. W. Pommerenke et al., RF design of traveling-wave accelerating structures for the FCCee injector complex, https://accelconf.web.cern.ch/linac2022/papers/thpojo08.pdf
  - N. Vallis et al., The PSI Positron Production project, https://accelconf.web.cern.ch/linac2022/papers/tupori16.pdf

- FCC-ee Injector Studies Mini-Workshop, Nov 24–25, 2023, IJCLab, Orsay, Paris https://indico.ijclab.in2p3.fr/event/8920/

Collaborators

PSI:	P. Craievich, B. Auchmann, I. M. Besana, S. Bettoni, H. Braun, M. Duda D. Hauenstein, R. Ischebeck, P. Juranic, J. Kosse, F. Marcellini, G. L. Orlandi, M. Pedrozzi, J.-Y. Raguin, S. Reiche, S. Sanfilippo, M. Schaer, N. Vallis, R. Zennaro, all the technical groups involved in the P^3 experiment
IJCLab:	I. Chaikovska, F. Alharthi, V. Mytrochenko, R. Chehab
CERN:	A. Grudiev, W. Bartmann, M. Benedikt, M. Calviani, S. Doebert, Y. Duthell, J. L. Grenard, B. Humann, A. Latina, A. Lechner, K. Oide, A. P. Marcone, R. Ramjiawan, Y. Zhao, R. Mena Andrade, Z. Vostrel, F. Zimmermann
INFN-LNF:	C. Milardi, A. De Santis, O. Etisken, S. Spampinati
KEK:	Y. Enomoto, K. Furukawa